ISAC-Enabled Low-Overhead Beam Management: Performance Analysis and Pilot Optimization

Yunchuan Huang, *Graduate Student Member, IEEE,* Jiajie Xu, Mihai A. Badiu, *Member, IEEE,* Gaojie Chen, Justin Coon, *Senior Member, IEEE,* and Mohamed-Slim Alouini, *Fellow, IEEE*

***Abstract*—The wealth of spectral resources in millimeter-wave (mmWave) and terahertz (THz) bands has the potential to support data transmission with Gbps, yet the narrow beams required at these frequencies introduce critical challenges in beam management. This paper investigates the application of integrated sensing and communications (ISAC) in the fifth-generation (5G) and beyond networks. By configuring synchronization signal blocks (SSB) and positioning reference signals (PRS), the proposed ISAC scheme enables intelligent inter-cell handovers and adaptive beam alignment for mobile terminals (MTs). With the tools from stochastic geometry, we first develop a unified analytical framework that yields tractable expressions for sensing and communication coverage probability and beam misalignment probability, explicitly capturing blockage process, beam dynamics, and multi-cell interference. Subsequently, we derive the optimal pilot design pattern that minimizes the beam misalignment probability. Taking into account both coverage performance and beam management overhead, the effective area spectral efficiency (ASE) metric is proposed to quantify the network-level benefits of ISAC. In addition, Monte Carlo simulation results are introduced to validate the theoretical analysis. Our study demonstrates that the proposed ISAC scheme can effectively enhance the ASE of the network and reduce the beam management overhead, especially in scenarios of dense base station (BS) deployments and large beam numbers. Furthermore, a fundamental beamwidth tradeoff is revealed: Although narrower beams improve the coverage for sensing, they can increase mobility-induced misalignment probabilities for communications. These insights provide concrete guidelines for practical ISAC-assisted beam management in future networks.**

***Index Terms*—Beam management, integrated sensing and communications (ISAC), stochastic geometry, 5G new radio**

I. Introduction

A. Background and Motivation

FUTURE sixth-generation (6G) communication networks are envisioned to support massive data services [1]. As crucial enablers, the millimeter wave (mmWave) and THz bands [2] have demonstrated their ability to offer multi-gigabit data rates. Unfortunately, these high-frequency bands also face critical physical challenges, such as high path loss, atmospheric attenuation, and susceptibility to blockages [3], which limit the coverage of high-frequency cells to relatively short ranges and require highly directional beams to maintain link quality. In this context, the use of narrow beams introduces new challenges related to beam management, including initial beam alignment, beam tracking, and beam recovery, which inevitably impose inherent costs on system overheads [4].

Meanwhile, integrating radar sensing into communication networks has been recognized as a future trend in 6G networks, termed integrated sensing and communications (ISAC). Thanks to the abundant spectral resources at mmWave and THz bands, radar sensing can be realized with precise range resolution for object detection, thereby facilitating opportunities for emerging applications, such as meta-verse, vehicle-to-infrastructure (V2I) networks, and smart cities [5, 6].

One of the most promising use cases of ISAC lies in *sensing-aided communications*, which refers to a paradigm where sensing capability is utilized to enhance communication quality-of-service (QoS) [7]. As a primary focus, sensing-aided communication beam management schemes have drawn intensive research interest. On the one hand, ISAC-assisted base stations (BSs) can obtain the position information of mobile terminals (MTs) without the conventional channel state information (CSI) acquisition, significantly saving beam alignment overhead. For example, the MT localization can be obtained by a factor-based algorithm in BS [8]. Following that spirit, the authors of [9] propose an extended Kalman filter (EKF) for user tracking in the ISAC-V2I system, and [10] shows that 43% beam management overheads can be reduced under the 5G new radio (NR) ISAC framework. On the other hand, by the detect-and-predict scheme, ISAC networks are expected to enable seamless BS handovers before link blockages, which can enhance overall network reliability. The typical work in [11] investigates radar-aided proactive blockage prediction based on the real-world dataset. However, although substantial efforts have been made to advance techniques, how much *network-level performance gain* can be achieved by the ISAC-enabled beam management scheme compared to conventional communication-only networks remains an unresolved question.

To answer this question, we adopt tools from stochastic geometry (SG) theory to analyze the network-level benefit of ISAC in a realistic beam management scheme. Naturally, this work aims to illustrate how sensing can benefit communications and quantify the coverage probability, overhead, and spectral efficiency in ISAC networks with physical imperfections.

Yunchuan Huang, Mihai A. Badiu, and Justin Coon are with the Department of Engineering Science, University of Oxford, Oxford, United Kingdom, OX1 3PJ (e-mails: {yunchuan.huang, mihai.badiu, justin.coon}@eng.ox.ac.uk). Jiajie Xu and Mohamed-Slim Alouini are with the Computer, Electrical, and Mathematical Science and Engineering (CEMSE) Division in King Abdullah University of Science and Technology (KAUST), Thuwal 6900, Makkah Province, Saudi Arabia (e-mails: {jiajie.xu.1, slim.alouini}@kaust.edu.sa). Gaojie Chen is with the School of Flexible Electronics, Sun Yat-Sen University, Shenzhen, China (e-mail: chengj235@mail.sysu.edu.cn).

This material is based upon work supported in part by the U. S. Army Research Laboratory and the U.S. Army Research Office under contract/grant number W911NF-24-2-0102, and in part by the Clarendon Scholarship.

B. Related Work

Research into the performance analysis of ISAC networks is still in its infancy. In particular, from an information-theoretic point of view, the literature [12] focuses on the fundamental limits of ISAC systems in a state-dependent delay feedback case. Applying this rationale to a Gaussian channel, the authors [13] investigate the performance tradeoffs between the Cramer-Rao bound (CRB) in sensing and the Shannon rate in communications. Subsequently, this framework has been extended to the analysis with various performance metrics, such as detection probability, detection rate, or degrees of freedom [14]. The work in [15] extends to cooperative ISAC networks, where the terminals share both data and extracted state information with each other.

As a powerful analytical tool, SG provides a general framework for modeling ISAC networks comprising BSs and MTs, enabling the derivation of key insights into their stochastic behavior. The authors in [16] provide tractable expressions for the coverage probability and rate metrics of a mmWave ISAC network in the presence of directional antennas and interference, [17] further derive the joint coverage probability and investigate the effect of the transmit power and the spectral allocation strategy, while the effects on BS density, blockage, and beamwidth are discussed in [18] and [19]. Furthermore, in [20], a cooperative multicell ISAC network with multiple users and sensing objects is analyzed, where the authors investigate the spectral efficiency and the optimal cluster size of BS.

Based on the performance analysis under the general framework, the feasibility and potential of incorporating ISAC into existing radio access network (RAN) standards also attract intensive research interest. The literature [21] provides an overview of ISAC signal design based on 5G, 5G-Advanced, and 6G systems. Based on the 5G-NR standard, [22] discusses the possibility of using the synchronization signal block (SSB), positioning reference signal (PRS), and demodulation reference signal (DMRS) to enable wireless sensing, validating their range and Doppler sensing capabilities. [23] proposes to use orthogonal frequency division multiplexing (OFDM) waveform in 5G-NR to refine the target localization, with a detailed analysis of the tradeoff between sensing and communications.

Despite the integrative nature of ISAC, most existing research analyzes sensing and communication sub-functions in isolation, thereby neglecting the coordination objective central to ISAC's original vision, especially in scenarios involving sensing-assisted beamforming. In addition to those we mentioned above, a recent work [24] proposes a new framework for sensing-aided beam training in a multi-input multi-output (MIMO) system which provides more accurate CSI for communication users, and [25] shows that the protocol they designed can achieve high-resolution positioning for communication beamforming, with communication and sensing performance boosted simultaneously. In terms of SG analysis, the most pertinent study in [26] examines the probability of beam misalignment in a 5G-NR-based ISAC system, and the authors further delve into the coverage performance in [27]. Although their work largely pushes the boundaries of ISAC, it does not consider practical issues such as delay requirements, sensor inaccuracies, the effects of clutter and interference, and how these affect overall system performance. Furthermore, as a major concern of network operators, the beam management overhead of ISAC-enabled schemes remains unaddressed in existing efforts.

C. Contributions

To the best of our knowledge, this work is the first to reveal the network-level performance gain of using ISAC. We address the challenges above by delving into an ISAC-enabled beam management framework for future mmWave/THz cellular networks. The key contributions of this work are summarized as follows:

(1) We propose a novel and practical ISAC-enabled network frame structure that supports unified OFDM waveform processing and seamless integration into existing RAN protocols. Specifically, the proposed sensing-aided beam management scheme incorporates dedicated SSB signals for blockage detection and NR-compliant PRS signals for MT tracking, enabling proactive handovers and low-latency beam alignment. Unlike previous works that distribute pilots across all time slots, the proposed scheme embeds PRSs flexibly within the frame and separates them from data payloads, which significantly reduces the beam management overhead and hardware complexity.

(2) A unified stochastic geometry framework is developed to evaluate the ISAC network performance, which considers the blockage process, clutter, interference, and sensor inaccuracies. Compared with prior work, we bridge sensing and communication by deriving closed-form expressions for the ISAC-enabled beam misalignment probabilities. These results lead to tractable coverage and asymptotic behavior analysis, which overcome the limitations of separate performance analysis for sensing and communication. Moreover, to quantify the network-level coordination gain introduced by ISAC, the effective area spectral efficiency (ASE) metric is proposed taking into account beam management overhead.

(3) Regarding network deployment, we investigate the optimal design of pilot patterns and derive a closed-form solution for the resource allocation ratio. Subsequently, extensive Monte Carlo experiments and numerical results are used to validate our theory. Under representative scenarios, the proposed ISAC-enabled scheme elevates the ASE from the 0.48-1.53 Mbps range observed in communication-only networks to over 10 Mbps, demonstrating a substantial improvement in network throughput. Furthermore, it is revealed that both the BS density and the beam number exhibit individual optimal points, which delineates the feasible design region for ultra-dense ISAC networks.

The remainder of this paper is organized as follows. Section II presents the system model, including the network architecture, the beamforming model, and the proposed ISAC-enabled beam management scheme. Subsequently, Section III analyzes the sensing performance in terms of resolution, accuracy, and coverage. In Section IV, we discuss the communication coverage performance with the aid of sensing, followed by the optimal pilot pattern design, overhead, and ASE analysis. The

numerical results will be demonstrated and analyzed in Section V. Finally, Section VI draws a comprehensive conclusion. The key notations used in this paper are summarized in Table I.

TABLE I: Summary of Key Notations

Notation	Description
Φ_B, Φ_O	Set of locations of ISAC-BS and blockers
$\lambda_B, \lambda_O, r_O$	BS, blocker density, and blocker radius
r_i	Distance from typical MT to its ith closest BS
ℓ_i	The distance of serving BS to its ith closest BS
$\mathcal{L}, \mathcal{L}_{\rm rt}$	Path loss of single / round-trip propagation
α_L, α_N	LoS / NLoS path loss exponents
$R_{\rm M}$	The resolution cell of MT
v	The speed of MT
n_B, θ_B	Beam number and beamwidth angle
$\sigma_{\rm CT}, \sigma_{\rm M}$	Radar cross section of clutter and MT
$G_{\rm ml}, G_{\rm sl}, \rho$	Mainlobe / sidelobe gain, and their ratio
$B_{\rm PRS}, B_{\rm SSB}, B_{\rm cb}$	Bandwidth of PRS, SSB, and carrier
$N_{\rm re}, \delta$	PRS resource block number and time-frequency ratio
f_Δ, f_c	Subcarrier spacing and center frequency
$T_{\rm PRS}, T_{\rm SSB}, T_{\rm sym}$	Duration of PRS, SSB, and OFDM symbol
$\tau, \tau_{\rm RRC}, \tau_{\rm RACH}$	Regular SSB periodicity, RRC delay, and RACH delay
S_t, S_f	PRS time-domain and frequency-domain spacing
$V_{\max}$, $D_{\max}$	Maximum detectable velocity and range

II. System Model

A. Network and Propagation Model

As shown in Fig. 1, we consider a downlink outdoor cellular network, where dual-function ISAC-BSs follow a homogeneous Poisson point process (PPP) $\Phi_B \subset \mathbb{R}^2$ with intensity λ_B. The blockers form another independent PPP $\Phi_O \subset \mathbb{R}^2$ with an intensity of λ_O. The radius of blockers is r_O. For communications, we assume that each MT adopts the maximal receive power (MRP) rule to connect itself to the nearest available BS, leading to a Poisson-Voronoi tessellation in BS cells. Consider an MT moving in a direction at speed v and served by the closest BS. According to the Slivnyak theorem [28], this MT becomes the typical MT by averaging over the PPP, which reflects the average receiver performance for the described network.

In the described network, the presence of blockages dictates whether the channel model is line-of-sight (LoS) or non-line-of-sight (NLoS) [29]. For the path with a distance r, the LoS probability between the BS and the MT is given by $p_L(r) = e^{-\beta r}$ and the NLoS probability is $p_N(r) = 1 - e^{-\beta r}$, where $\beta = 2\lambda_O r_O$ is the blockage effect parameter depending on the density and shape of the blocks. Considering the propagation characteristics of the mmWave/THz bands, the path loss between MT and BS at distance r follows a Boolean scheme [1]:

$$\mathcal{L}(r) = \left[c/(4\pi f_c)\right]^2 r^{-\alpha_u}, \quad \text{w.p.} \quad p_u(r), u \in \{L, N\}. \quad (1)$$

where c is the speed of light, and f_c the carrier frequency. The parameters α_L and α_N are the path loss exponents of the LoS and NLoS channel. Specifically, in the sensing functionality, the round-trip echo path loss from BS to MT can be derived by the radar function [31]

$$\mathcal{L}_{\rm rt}(r) = \mathcal{L}(r^2)/4\pi. \quad (2)$$

B. Beamforming Model

We consider a sectorized antenna model, where each BS uses directional antennas with beam number n_B, each sector indicating the main lobe of the BS beam with a beamwidth of $\theta_B = 2\pi/n_B$. This setup allows MT to experience beam switch points during movement. According to the properties of Voronoi tessellation, the beam switch points have a Poisson distribution with an intensity $\mu_g = (n_B\sqrt{\lambda_B})/\pi$ [4]. The distance between two beam switch points d_b follows the exponential distribution with mean $1/\mu_g$. The antenna gain is given by grid-of-beams (GoB) model as follows

$$G(\phi) = \begin{cases} G_{\rm ml}, & \text{if } |\phi| \le \theta_B/2, \\ G_{\rm sl}, & \text{otherwise}, \end{cases} \quad (3)$$

where ϕ is the angle off the boresight direction of the BS. $G_{\rm ml}$ and $G_{\rm sl}$ are constants. Specifically, we assume that each MT has an isotropic antenna with unit gain. The mainlobe-to-sidelobe ratio (MSLR) is given by $\rho = G_{\rm ml}/G_{\rm sl}$. This paper assumes a squared beamforming gain law[2] that $\rho = n_B^2$ [4].

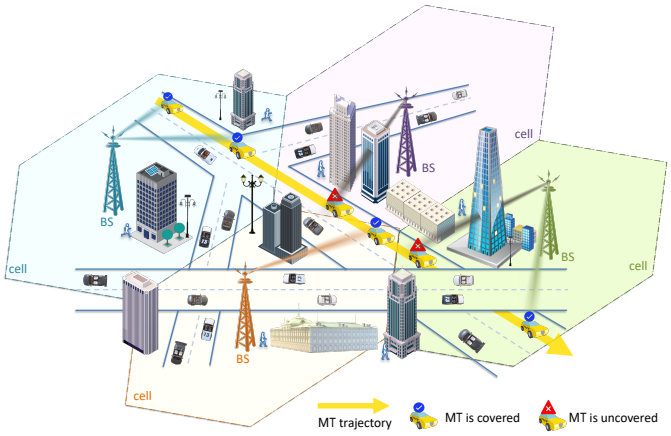

Fig. 1: The depicted ISAC system model.

C. ISAC-Enabled Beam Management Scheme

1) Frame Structure: As shown in Fig. 2, the proposed downlink 5G-ISAC system incorporates the sensing and communication capability in the unified OFDM waveform. The frame consists of SSB bursts and data blocks.

SSB bursts are periodically transmitted with a regular periodicity τ (20 ms by default), allowing BS to perform a beam

[1]While the Boolean disc model does not describe the exact geometry of real urban buildings, it captures the primary effect of blockage and is widely adopted in stochastic geometry analysis of mmWave/THz systems [29, 30] as the key blockage effect is summarized by the LoS probability. More complex propagation environments with correlated shadowing or irregular buildings mainly change the parameter β and hence shift the optimal BS density and beam number, but do not alter other qualitative tradeoffs revealed by our subsequent analysis.

[2]The assumptions of isotropic MT antennas and the ideal scaling law $\rho = n_B^2$ serve as theoretical baselines for tractability. In practice, dual-sided beamforming at the MT increases sensitivity to misalignment, while RF impairments cause gain saturation (a gain plateau) at large n_B [32]. Both factors imply that the diminishing returns of beam narrowing manifest earlier than in our model. Thus, the identified trade-off between gain and reliability remains valid and becomes even more critical in realistic deployments.

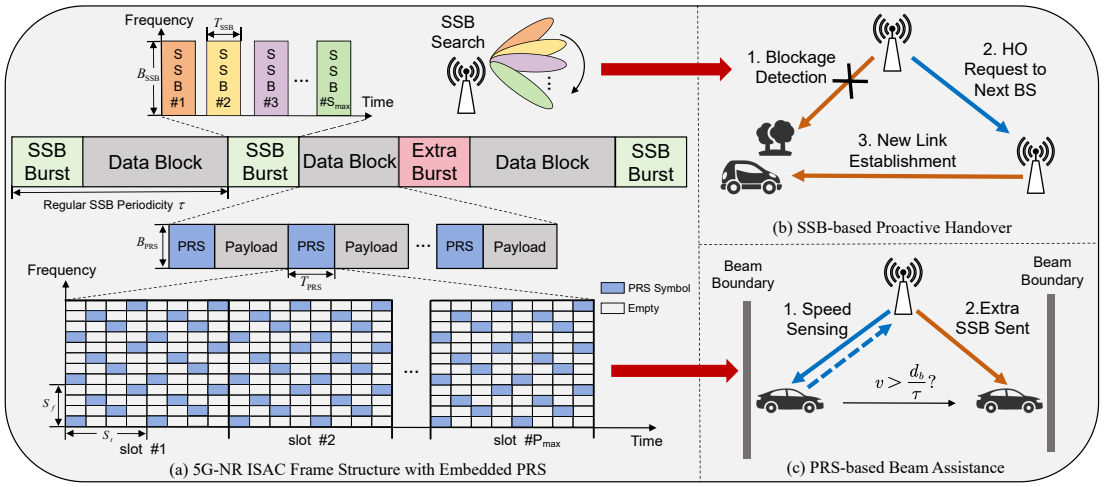

Fig. 2: ISAC-Enabled 5G downlink frame design and adaptive beam management procedures.

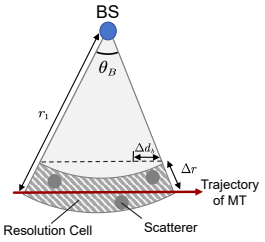

Fig. 3: The sensing resolution cell.

search and establish initial access, and extra bursts that can be dynamically inserted when beam assistance is required. There are a series of SSBs in each burst, and one SSB occupies a bandwidth of B_{SSB} and spans a time duration of T_{SSB}.

The primary advancement of the proposed ISAC scheme lies in the sensing signal patterns. Specifically, different from [27] that spreads pilots throughout all time slots, we propose a flexible embedding of NR-compliant PRS within data blocks, separated from payload data, to enable high-accuracy localization and mobility-aware beam management. Depending on different use scenarios, the PRS signal can be dynamically configured to be active or mute within a data block. Each PRS block has a bandwidth of B_{PRS} with a subcarrier spacing of S_f and a time duration of T_{PRS} with an OFDM symbol spacing of S_t, respectively. Given the total number of pilots, the proposed scheme can efficiently mitigate the beam management overhead and the fast Fourier transform (FFT) complexity due to the dynamic design principle.

2) Beam Management Procedures: Both PRS and SSB signals can enable wireless sensing and extraction of environmental information, as they have ideal autocorrelation properties [22, 33]. The proposed ISAC-based beam management procedures use both SSB and PRS signals to enhance handover and beam alignment, as illustrated in Fig. 2(b) and Fig. 2(c), respectively.

- **SSB-Based Proactive Handover**: SSB signals can cover all directions during the beam search procedure, making them suitable for blockage detection with periodically updated information. In the proposed scheme, the system continuously monitors link quality and detects potential blockages. Upon the detection of a blockage, a handover (HO) request is proactively sent to the next available BS. The new BS establishes a connection with the MT before the link with the previous BS deteriorates completely for seamless connectivity.
- **PRS-Based Beam Assistance**: PRS can span a longer time duration with wide bandwidth and provide better Doppler and range estimation. In the proposed scheme, the PRS is dedicated to sense the typical MT's speed and predict its future location relative to the beam boundaries. If the BS realizes that the MT is moving too fast to receive at least one SSB burst between two beam boundaries, an additional SSB burst will be transmitted immediately to assist with beam alignment and mitigate the risk of link failure.

Remark 1. From an implementation perspective, the PRS-based speed and range estimation at the BS relies on FFT-based processing and peak detection within each PRS block, which is already supported by NR positioning procedures [22, 31, 34]. Predicting beam-boundary crossings only requires linear motion extrapolation per tracked UE, so the computational complexity scales almost linearly with the number of PRS tracks. Furthermore, the proposed extra SSB mechanism can be practically implemented using aperiodic CSI-RS resources configured for beam management, which supports flexible sub-slot scheduling. While Fig. 2 conceptually aligns the sensing and training phases, practical scheduling involves a processing timeline and Physical Downlink Control Channel (PDCCH) overhead (e.g., the Downlink Control Information, DCI) to trigger these aperiodic signals [33]. This control overhead is generally small compared to the data payload.

D. Sensing Model

Wireless sensing performance depends on the radar cross section (RCS), which quantifies the ability of a target to reflect radar signals back to the receiver. To model the RCS of the MT and clutter, we adopt the Swerling I model [35] as it effectively characterizes targets with slow amplitude fluctuations, such as pedestrians and vehicles, which aligns with the typical mobility scenarios in cellular networks. Specifically, the RCS of the MT, denoted as σ_{M}, and the RCS of clutter, σ_{CT}, both

follow an exponential distribution, i.e., $\sigma_{\mathrm{M}}, \sigma_{\mathrm{CT}} \sim \exp(1)$. Let the serving BS be located at the origin, let r_1 be the distance between the MT and the serving BS, and express the desired sensing signal power

$$\mathrm{Signal}_{\mathrm{S}} = P_{\mathrm{S}} G_{\mathrm{ml}} \sigma_{\mathrm{M}} \mathcal{L}_{\mathrm{rt}}(r_1), \tag{4}$$

where P_{S} is the sensing transmit power, and G_{ml} is the sensing antenna gain [3].

In our setup, network blockers act as scatterers, introducing unexpected clutter signals that affect wireless sensing. As shown in Fig. 3, we assume that clutter is generated solely by scatterers located within the same *resolution cell* as the typical MT, and only the clutter caused by single reflections is considered [4]. Using the radar equation [37], the aggregate clutter power (Watts) at the serving BS (referred to as BS_0) can be written as

$$CT_{\mathrm{S}} = \textstyle\sum_{ct \in \{R_{\mathrm{M}}\}} P_{\mathrm{S}} G_{\mathrm{S}} \sigma_{\mathrm{CT}} \mathcal{L}_{\mathrm{rt}}(r_{ct}), \tag{5}$$

where $r_{ct} \approx r_1$ is the scatter distance, and R_{M} is the beam-wise resolution cell of MT. Specifically, given the radar range resolution Δr and beamwidth θ_B, R_{M} has an area of $A(R_{\mathrm{M}}) \approx \Delta r \times \theta_B \times r_1$.

Additionally, the aggregate sensing interference signal directly received from other BSs can be written as

$$I_{\mathrm{S}} = \textstyle\sum_i P_{\mathrm{S}} h_i \mathcal{L}(\ell_i) G_{\mathrm{S}}^{\mathrm{I}}(\phi_i), \tag{6}$$

where ℓ_i is the distance between BS_0 and the ith closest interfering BS, $h_i \sim \exp(1)$ is the small-scale Rayleigh fading channel coefficient, and $\phi_i \sim U[0, 2\pi]$ is the boresight angle of the i-th BS, with a gain of $G_{\mathrm{S}}^{\mathrm{I}}(\phi_i)$. Since the sensing interference occurs only when the interfering beam is aligned with the serving beam [27], the interference probability is

$$\mathbb{P}(G_{\mathrm{S}}^{\mathrm{I}}(\phi_i) = G_{\mathrm{ml}}) = (\theta_B/2\pi)^2 = 1/n_B^2.$$

Otherwise, $G_{\mathrm{S}}^{\mathrm{I}}(\phi_i) = G_{\mathrm{sl}}$.

Assume that path loss, fading coefficients, and boresight angles are i.i.d. for all paths. In view of severe interference in dense cell deployments, we consider an interference-limited network and neglect noise [20]. Therefore, the signal-to-clutter-and-interference ratio (SCIR) is adopted as the primary performance metric for wireless sensing, which is given by

$$\mathrm{SCIR}_{\mathrm{S}} = \frac{\mathrm{Signal}_{\mathrm{S}}}{CT_{\mathrm{S}} + I_{\mathrm{S}}}. \tag{7}$$

E. Communication Model

The signal-to-interference ratio (SIR) is introduced to describe downlink communications. Let the typical MT be at the origin, and let the ith closest BS (BS_i) be with some distance r_i. We formulate the SIR for the conventional scheme without sensing functionality, and the SIR for the proposed ISAC scheme.

1) Conventional Scheme: For conventional communication-only networks, the downlink SIR at the MT side is given by

$$\mathrm{SIR}_{\mathrm{C}}^{\mathrm{w/o}} = \frac{P_{\mathrm{C}} h_1 G_{\mathrm{C}} \mathcal{L}(r_1)}{I_{\mathrm{C}}}, \tag{8}$$

where P_{C} is the communication transmit power, $h_1 \sim \exp(1)$ is the Rayleigh fading factor, and G_{C} represents the communication beamforming gain, which is a random variable dependent on beam alignment. According to 3GPP specifications, each MT must receive at least one SSB burst between two beam boundaries to evaluate beam quality and select the best beam [4]. If the MT moves too fast, it may remain temporarily connected to the previous reference beam through its sidelobes. This mobility-induced beam misalignment occurs when the beam boundary distance satisfies $d_b < v\tau$. Given that $d_b \sim \exp(\mu_g)$, the average misalignment probability is $p_{\mathrm{mis}} = 1 - \exp(-\mu_g v\tau)$. Consequently, the communication beamforming gain G_{C} can be written as

$$G_{\mathrm{C}} = \begin{cases} G_{\mathrm{ml}}, & \text{w. p.} \quad \exp(-\mu_g v\tau), \\ G_{\mathrm{sl}}, & \text{w. p.} \quad 1 - \exp(-\mu_g v\tau). \end{cases} \tag{9}$$

The communication interference term I_{C} includes the interference from other communication BSs, which is given by

$$I_{\mathrm{C}} = \textstyle\sum_{i>1} P_{\mathrm{C}} h_i \mathcal{L}(r_i) G(\phi_i), \tag{10}$$

where $\phi_i \sim U[0, 2\pi]$, and $G(\cdot)$ is the interfering beamforming gain given by (3).

2) Sensing-aided Communications: The SIR performance in ISAC-enabled systems is governed by two critical factors:

- **Handover Timeout:** Following the 5G NR specifications, the radio resource control (RRC) delay $\tau_{\mathrm{RRC}} = 3$ ms establishes a hard threshold [34] for the handover response. The timeout occurs if the MT speed satisfies $d_b < v\tau_{\mathrm{RRC}}$ (defined as event $\mathcal{A}$). In this case, neither proactive handover nor beam assistance can be completed before beam boundary crossing, so MT can only connect to BS_1 with its sidelobe gain.
- **PRS Sensing Error:** Assuming the blockage detection results by periodic SSB bursts are accurate [5], the PRS-based speed estimation inaccuracy may cause erroneous beam coordination decisions. Specifically, this happens when the BS underestimates the MT speed and misjudges that MT can receive the scheduled SSB burst (defined as event $\mathcal{B}$), which eventually results in communication beam misalignment.

Allowing for the two factors above, the SIR of MT in our

[3]This paper focuses on a sensing-aided communication system, where we assume a fixed beamforming gain for radar sensing. This assumption is valid when the radar employs a predefined scanning beam [36].

[4]The assumption focuses on the scatterers within the illuminated resolution cell to capture the dominant clutter power [19]. While practical urban sensing may involve distributed clutter received through antenna sidelobes, these components are significantly suppressed by the spatial filtering of narrow beams ($G_{\mathrm{sl}} \ll G_{\mathrm{ml}}$). Moreover, in the considered dense cellular network, the system performance is primarily interference-limited. Consequently, the residual sidelobe clutter is negligible compared to the strong aggregate inter-cell interference and is therefore omitted to facilitate tractable analysis.

[5]It is noted that practical blockage detection via SSB bursts may suffer from missed detections or false alarms. However, given the robust detection capability of SSB signals [26, 27], these errors are generally less frequent compared to handover timeouts and sensing-induced beam misalignments. This assumption is to maintain analytical tractability and focus on the critical impacts of sensing accuracy and latency.

depicted ISAC network is

$$\mathrm{SIR}_{\mathrm{C}}^{\mathrm{isac}} = \mathbb{1}_{\{\mathcal{A}\}}\mathrm{SIR}_{\mathrm{sl}}^{1} + \mathbb{1}_{\{\overline{\mathcal{A}}\cap\mathcal{B}\}}\mathrm{SIR}_{\mathrm{sl}}^{k^*} + \mathbb{1}_{\{\overline{\mathcal{A}}\cap\overline{\mathcal{B}}\}}\mathrm{SIR}_{\mathrm{ml}}^{k^*}. \quad (11)$$

In (11), the first term corresponds to the SIR without handover and beam assistance, the second reflects the SIR involving proactive handover but without beam assistance (due to sensing error), and the third term reflects the SIR with both handover and accurate beam assistance, respectively. $\mathbb{1}_{\{\cdot\}}$ denotes the indicator function, $\overline{\mathcal{A}}$ denotes the complement of event $\mathcal{A}$, $\mathrm{SIR}_{\Omega}^{k} \triangleq P_{\mathrm{C}}G_{\Omega}h_k\mathcal{L}(r_k)/I_{C,k}$, $\Omega \in \{\mathrm{ml}, \mathrm{sl}\}$, and $k^* \triangleq \underset{k\in\{1,2\}}{\arg\max}\,\mathcal{L}(r_k)$ selects the BS with the stronger path gain. Particularly, the BS-wise interference term in the ISAC network is given by

$$I_{C,i} = \textstyle\sum_{j>1, j\neq i} P_{\mathrm{C}}h_j\mathcal{L}(r_j)G(\phi_j). \quad (12)$$

Note that the interference term $I_{C,2}$ excludes the contribution of BS_1. This is because BS_1 proactively mutes itself during handover to mitigate interference.

Remark 2. (11) indicates that the communication performance relies on the sensing performance in the depicted ISAC network, as the received SCIR for sensing determines whether errors occur in MT speed and location estimates, finally leading to beam alignment or misalignment.

III. Sensing Performance

This section analyzes the sensing performance of the depicted ISAC network in two respects. First, the resolution and maximum detectable range/velocity of PRS sensing will be introduced, with an emphasis on the relationship between resolution and accuracy. Second, we will describe the coverage probability using the SG tools.

A. Resolution and Accuracy

Since the PRS is dedicated to MT tracking, its resolution dictates the minimum change that can be detected. Specifically, for a PRS block with bandwidth B_{PRS}, time duration T_{PRS}, and carrier frequency at f_c, its radial range resolution Δr and velocity resolution Δv can be expressed by [37]

$$\Delta r = c/2B_{\mathrm{PRS}}, \Delta v = c/2f_cT_{\mathrm{PRS}}, \quad (13)$$

where c is the speed of light. As shown in Fig. 3, the relationship between the motion resolution Δd_b and the radial resolution Δr can be modeled as $\Delta d_b = 2\Delta r\sin(\theta_B/2) = 2\Delta r\sin(\pi/n_B)$.

Furthermore, the maximum detectable range and velocity of PRS also dictate the radar capability. According to OFDM radar principles, the maximum detectable range of a radar (denoted as $d_{\max}$) is determined by PRS subcarrier spacing S_f, while the maximum detectable velocity $v_{\max}$ is determined by PRS spacing S_t [38]

$$d_{\max} = c/2S_f f_\Delta, v_{\max} = c/2S_tT_{\mathrm{sym}}f_c. \quad (14)$$

where f_Δ is the OFDM subcarrier spacing, and T_{sym} is the duration of the OFDM symbol.

As mentioned above, the sensing error can lead to incorrect beam alignment decisions. To describe the error in MT tracking, we consider an additive white Gaussian noise (AWGN) model, where the estimated speed $\hat{v}$ and the estimated lateral motion $\hat{d}_b$ are given by $\hat{v} = v + \epsilon_v, \hat{d}_b = d_b + \epsilon_d$, where $\epsilon_v \sim \mathcal{N}(0, \sigma_v^2), \epsilon_d \sim \mathcal{N}(0, \sigma_d^2)$ are the sensing errors and can be regarded as independent random variables [39]. Specifically, the speed accuracy and motion accuracy depend on both their resolutions and the sensing SCIR [36]:

$$\sigma_v^2 = (\Delta v)^2/(4\pi^2\cdot\mathrm{SCIR}_{\mathrm{S}}), \sigma_d^2 = 2(\Delta d_b)^2/\mathrm{SCIR}_{\mathrm{S}}, \quad (15)$$

where $\mathrm{SCIR}_{\mathrm{S}}$ is given by (7), and σ_v and σ_d are the root mean square values (RMS) of the difference between the estimated value of speed and motion and their true values.

B. Coverage Probability Characterization

The sensing SCIR coverage probability at a given threshold $\eta > 0$ is defined as

$$p_{\mathrm{cov,S}}(\eta; \lambda_B, \lambda_O, n_B) \triangleq \mathbb{P}(\mathrm{SCIR}_{\mathrm{S}} > \eta), \quad (16)$$

where the expression of $\mathrm{SCIR}_{\mathrm{S}}$ is given in (7).

Theorem 1. (Sensing Coverage Probability) Conditioning on the distance between MT and the closest BS r_1, the sensing coverage probability in the depicted ISAC network is given by

$$\begin{aligned} &p_{\mathrm{cov,S}|r_1}(\eta|r_1) = \mathbb{P}\left(\mathrm{SCIR}_{\mathrm{S}} > \eta | r_1\right) \\ &= F_{ct}(\eta|r_1)\left[p_L\left(r_1\right)F_{S,L}(\eta|r_1) + p_N\left(r_1\right)F_{S,N}(\eta|r_1)\right], \end{aligned} \quad (17)$$

where

$$\begin{aligned} F_{ct} &= \exp\left(-\frac{2\pi\eta\lambda_O r_1\Delta r}{n_B(1+\eta)}\right), \\ F_{S,L} &= \exp\left[-2\lambda_B\pi\int_0^\infty w\left(1 - Q\left(\eta, w, r_1^{2\alpha_L}\right)\right)\mathrm{d}w\right], \\ F_{S,N} &= \exp\left[-2\lambda_B\pi\int_0^\infty w\left(1 - Q\left(\eta, w, r_1^{2\alpha_N}\right)\right)\mathrm{d}w\right]. \end{aligned} \quad (18)$$

The function $Q(\cdot,\cdot,\cdot)$ is given by

$$\begin{aligned} Q\left(\eta, w, r_1^{2\alpha}\right) &= p_L(w)\left[\frac{w^{\alpha_L}}{n_B^2(w^{\alpha_L} + 4\pi\eta r_1^{2\alpha})} + \frac{\rho w^{\alpha_L}(n_B^2 - 1)}{n_B^2(\rho w^{\alpha_L} + 4\pi\eta r_1^{2\alpha})}\right] \\ &+ p_N(w)\left[\frac{w^{\alpha_N}}{n_B^2(w^{\alpha_N} + 4\pi\eta r_1^{2\alpha})} + \frac{\rho w^{\alpha_N}(n_B^2 - 1)}{n_B^2(\rho w^{\alpha_N} + 4\pi\eta r_1^{2\alpha})}\right]. \end{aligned} \quad (19)$$

Proof. See Appendix A. □

Accordingly, the unconditional sensing coverage probability can be derived by averaging over r_1

$$p_{\mathrm{cov,S}} = \mathbb{E}_{r_1}[p_{\mathrm{cov,s}|r_1}] = \int_0^\infty p_{\mathrm{cov,s}|r_1}(\eta|r_1) f_{r_1}\left(r_1\right)\mathrm{d}r_1, \quad (20)$$

where $f_{r_1}(r) = 2\lambda_B\pi re^{-\lambda_B\pi r^2}$ is the probability density function (PDF) of r_1 in a PPP setup. Furthermore, the PDF of sensing SCIR can be written as

$$f_{\mathrm{SCIR}}(\eta) = \frac{\partial}{\partial\eta}[1 - p_{\mathrm{cov,S}}\left(\eta; \lambda_B, \lambda_O, n_B\right)]. \quad (21)$$

We now characterize the asymptotic behavior of the sensing coverage probability by a special but illustrative case.

Corollary 1. (SCIR Coverage, Special Case) When $\alpha_L = \alpha_N = \alpha > 2$, MSLR $\rho = n_B^2$, for a large beam number n_B,

one can approximate the sensing coverage probability (20) by a closed-form expression

$$\begin{aligned} p_{\mathrm{cov,S}} &\approx \frac{\pi\sqrt{\pi}n_B^{\frac{2}{\alpha}}}{2\eta^{\frac{1}{\alpha}}\gamma}\exp\left(\frac{\lambda_B\pi^2 n_B^{\frac{4}{\alpha}}}{4\eta^{\frac{2}{\alpha}}\gamma}\right)\mathrm{erfc}\left(\frac{\sqrt{\lambda_B}\pi n_B^{\frac{2}{\alpha}}}{2\eta^{\frac{1}{\alpha}}\sqrt{\gamma}}\right) \\ &\overset{(a)}{=} 1-\frac{2\gamma\eta^{\frac{2}{\alpha}}}{\lambda_B\pi^2 n_B^{\frac{4}{\alpha}}}+\mathcal{O}\left(n_B^{-\frac{8}{\alpha}}\right), \end{aligned} \tag{22}$$

where $\mathrm{erfc}(\cdot)$ is the complementary error function, the constant $\gamma = \frac{2\pi}{\alpha}\Gamma\left(\frac{2}{\alpha}\right)\Gamma\left(1-\frac{2}{\alpha}\right)(4\pi)^{\frac{2}{\alpha}}$, and $\Gamma(\cdot)$ is the Gamma function.

Proof. In such a case, it follows that $F_{S,L} = F_{S,N} \triangleq F_S$. On the other hand, for a large n_B, $F_{ct} \approx 1$, so (19) can be approximated by $Q \approx \rho w^{\alpha}/(\rho w^{\alpha} + 4\pi\eta r_1^{2\alpha})$. Using the squared MSLR $\rho = n_B^2$, (17) is reduced to

$$\begin{aligned} p_{\mathrm{cov,S}|r_1} &\approx F_S = \exp\left[-2\lambda_B\pi\int_0^{\infty}\frac{4w\pi\eta r_1^{2\alpha}}{n_B^2 w^{\alpha}+4\pi\eta r_1^{2\alpha}}\mathrm{d}w\right] \\ &\overset{(b)}{=} \exp\left[-2\lambda_B\pi\frac{1}{\alpha}\left(\frac{4\pi\eta r_1^{2\alpha}}{n_B^2}\right)^{\frac{2}{\alpha}}\Gamma\left(\frac{2}{\alpha}\right)\Gamma\left(1-\frac{2}{\alpha}\right)\right] \\ &= \exp\left[-\gamma\lambda_B\eta^{\frac{2}{\alpha}}n_B^{-\frac{4}{\alpha}}r_1^4\right], \end{aligned} \tag{23}$$

where (b) holds when $\alpha > 2$ (see (4.11) in [40]), and (a) comes from the asymptotic expansion formula $\mathrm{erfc}(x) = \frac{1}{x\sqrt{\pi}}e^{-x^2}\left(1-\frac{1}{2x^2}+\mathcal{O}\left(\frac{1}{x^4}\right)\right)$. Plugging this result into (20) gives the expression in the first line of (22). □

Remark 3. Note that in (22), the sensing coverage probability $p_{\mathrm{cov,S}}$ grows monotonically with n_B, and $p_{\mathrm{cov,S}} \to 1$ as $n_B \to \infty$. In fact, this trend still holds for a general case where $\alpha_N > \alpha_L \geq 2$, as shown in the numerical results. This can be explained by the round-trip path loss experienced by the desired sensing signal. Consequently, the sensing coverage performance benefits from the higher beamforming gain and the reduced clutter brought about by the larger beam numbers.

IV. Communication Performance

Communication performance will be detailed by three aspects. First, we derive a tractable expression for the conditional and unconditional communication coverage probability by event partitioning. Next, the optimal design of the PRS pilot that minimizes the beam misalignment probability is formulated and solved. Finally, the beam management overheads of the proposed ISAC scheme and conventional schemes are analyzed, introducing the metric of effective ASE.

A. Coverage Probability Characterization

The communication SIR coverage probability at a given threshold $\zeta > 0$ is defined as:

$$p_{\mathrm{cov,C}}^{\mathrm{isac}}(\zeta;\lambda_B,\lambda_O,n_B) \triangleq \mathbb{P}(\mathrm{SIR}_{\mathrm{C}}^{\mathrm{isac}} > \zeta), \tag{24}$$

where $\mathrm{SIR}_{\mathrm{C}}^{\mathrm{isac}}$ is given by (11). Recall that there are three exclusive terms in $\mathrm{SIR}_{\mathrm{C}}^{\mathrm{isac}}$, each corresponding to a conditional SIR expression. Using the partitioning theorem, we have

$$\begin{aligned} p_{\mathrm{cov,C}}^{\mathrm{isac}} &= \mathbb{P}[\mathcal{A}]\mathbb{P}[\mathrm{SIR}_{\mathrm{sl}}^{1} > \zeta] + \mathbb{P}[\overline{\mathcal{A}}\cap\mathcal{B}]\mathbb{P}[\mathrm{SIR}_{\mathrm{sl}}^{k^*} > \zeta] \\ &\quad + \mathbb{P}[\overline{\mathcal{A}}\cap\overline{\mathcal{B}}]\mathbb{P}[\mathrm{SIR}_{\mathrm{ml}}^{k^*} > \zeta]. \end{aligned} \tag{25}$$

Lemma 1. The timeout probability $\mathbb{P}[\mathcal{A}] \triangleq p_{\mathrm{to}} = 1 - \exp(-\mu_g v\tau_{\mathrm{RRC}})$.

Proof. The proof is similar to that shown in Section II-E1. □

Lemma 2. Let $0 < \mu_0 < \mu < +\infty$, and define random variables $X \sim \mathcal{N}(\mu,\sigma^2), Y \sim \exp(\mu_g)$, then the probability

$$\begin{aligned} &\mathbb{P}\{\max(X,\mu_0) < Y < \mu\} \triangleq q(\sigma;\mu_g,\mu_0,\mu) \\ &= \frac{e^{\frac{1}{2}\mu_g^2\sigma^2-\mu\mu_g}}{2}\left[\mathrm{erf}\left(\frac{\mu_g\sigma}{\sqrt{2}}\right)-\mathrm{erf}\left(\frac{\mu_0-\mu+\mu_g\sigma^2}{\sqrt{2}\sigma}\right)\right] \\ &+ \frac{e^{-\mu_0\mu_g}}{2}\mathrm{erf}\left(\frac{\mu_0-\mu}{\sqrt{2}\sigma}\right)+\frac{e^{-\mu_0\mu_g}-e^{-\mu\mu_g}}{2}. \end{aligned} \tag{26}$$

Proof. The event $\{\max(X,\mu_0) < Y < \mu\}$ is equivalent to $\{X < Y < \mu, Y > \mu_0\}$. Considering PDFs of X and Y along with the appropriate region of integration, the probability q can be calculated by

$$\begin{aligned} q(\sigma;\mu_g,\mu_0,\mu) &= \int_{\mu_0}^{\mu}\mathrm{d}y\int_{-\infty}^{y}\frac{e^{-\frac{(x-\mu)^2}{2\sigma^2}}}{\sqrt{2\pi\sigma^2}}\mu_g e^{-\mu_g y}\mathrm{d}x \\ &\overset{(a)}{=} \int_{\mu_0}^{\mu}\frac{1}{2}\left[1+\mathrm{erf}\left(\frac{y-\mu}{\sqrt{2\sigma^2}}\right)\right]\mu_g e^{-\mu_g y}\mathrm{d}y, \end{aligned} \tag{27}$$

where (a) is due to the cumulative distribution function (CDF) of the Gaussian distribution, and $\mathrm{erf}(\cdot)$ is the error function. When $a, b > 0$, we have [40]

$$\int \mathrm{erf}(ax)be^{-bx}\,\mathrm{d}x = e^{\frac{b^2}{4a^2}}\mathrm{erf}\left(\frac{2a^2x+b}{2a}\right)-e^{-bx}\mathrm{erf}(ax),$$

where the integration constant is omitted. Therefore, the integral in the last line of (27) finally yields (26). □

Theorem 2. (Conditional Communication Coverage) Conditioning on r_1 and sensing SCIR η, the communication coverage probability is given by

$$p_{\mathrm{cov,C}|r_1}^{\mathrm{isac}}(\zeta|\eta,r_1) = p_{\mathrm{to}}\mathcal{I}_1 + (1-p_{\mathrm{to}})\left[(1-p_v^s(\eta))\mathcal{I}_2 + p_v^s(\eta)\mathcal{I}_3\right], \tag{28}$$

where

$$p_v^s(\eta) = \min\left\{q(\sigma(\eta);\mu_g,\mu_0,\mu)e^{\mu_g\mu_0}, 1-e^{-\mu_g(\mu-\mu_0)}\right\} \tag{29}$$

is the sensing error-induced beam misalignment probability (conditioning on no timeout), with parameters given by

$$\sigma(\eta) = \sqrt{\tau^2\sigma_v^2(\eta)+\sigma_d^2(\eta)}, \mu_0 = \tau_{\mathrm{RRC}}v, \mu = \tau v. \tag{30}$$

Three conditional coverage probabilities are computed as

$$\begin{aligned} \mathcal{I}_1 &= p_L(r_1)\,U_{\mathrm{sl}}(\zeta, r_1^{\alpha_L}) + p_N(r_1)\,U_{\mathrm{sl}}(\zeta, r_1^{\alpha_N}), \\ \mathcal{I}_2 &= \int_{r_1}^{\infty} W_{\mathrm{ml}}(r_2;r_1) f_{r_2|r_1}(r_2)\,\mathrm{d}r_2, \\ \mathcal{I}_3 &= \int_{r_1}^{\infty} W_{\mathrm{sl}}(r_2;r_1) f_{r_2|r_1}(r_2)\,\mathrm{d}r_2, \end{aligned} \tag{31}$$

where the conditional PDF of the second closest BS distance r_2 given r_1 is $f_{r_2|r_1}(r_2) = e^{-\lambda_B\pi\left(r_2^2-r_1^2\right)}2\lambda_B\pi r_2$, and the helper functions $W_{\Omega}, U_{\Omega}, R_{\mathrm{ml}}, R_{\mathrm{sl}}$ are given by (32) at the top of next page.

Proof. See Appendix B. □

Theorem 3. (Unconditional Communication Coverage) The expression for the unconditional communication coverage

$$W_\Omega(r_2;r_1)=p_L(r_1)\,U_\Omega(\zeta,r_1^{\alpha_L})+p_N(r_1)\left[p_L(r_2)\,U_\Omega(\zeta,r_2^{\alpha_L})+p_N(r_2)\,U_\Omega(\zeta,r_1^{\alpha_N})\right], \tag{32a}$$

$$U_\Omega(\zeta,r_k^\alpha)=\exp\left[-2\pi\lambda_B\int_{r_k}^{\infty}\left(1-R_\Omega(\zeta,w,r_k^\alpha)\right)w\mathrm{d}w\right],\Omega\in\{\mathrm{ml},\mathrm{sl}\},k\in\{1,2\},\alpha\in\{\alpha_L,\alpha_N\}. \tag{32b}$$

$$R_{\mathrm{ml}}(\zeta,w,r_k^\alpha)=p_L(w)\left(\frac{w^{\alpha_L}}{n_B\left(w^{\alpha_L}+\zeta r_k^\alpha\right)}+\frac{(n_B-1)\,\rho w^{\alpha_L}}{n_B\left(\rho w^{\alpha_L}+\zeta r_k^\alpha\right)}\right)+p_N(w)\left(\frac{w^{\alpha_N}}{n_B\left(w^{\alpha_N}+\zeta r_k^\alpha\right)}+\frac{(n_B-1)\,\rho w^{\alpha_N}}{n_B\left(\rho w^{\alpha_N}+\zeta r_k^\alpha\right)}\right). \tag{32c}$$

$$R_{\mathrm{sl}}(\zeta,w,r_k^\alpha)=p_L(w)\left(\frac{w^{\alpha_L}}{n_B\left(w^{\alpha_L}+\zeta\rho r_k^\alpha\right)}+\frac{(n_B-1)\,w^{\alpha_L}}{n_B\left(w^{\alpha_L}+\zeta r_k^\alpha\right)}\right)+p_N(w)\left(\frac{w^{\alpha_N}}{n_B\left(w^{\alpha_N}+\zeta\rho r_k^\alpha\right)}+\frac{(n_B-1)\,w^{\alpha_N}}{n_B\left(w^{\alpha_N}+\zeta r_k^\alpha\right)}\right). \tag{32d}$$

probability $p_{\mathrm{cov,C}}^{\mathrm{isac}}$ follows the form in (25), each term given by

$$\begin{aligned}&\mathbb{P}[\mathcal{A}]=p_{\mathrm{to}},\mathbb{P}[\mathrm{SIR}_{\mathrm{sl}}^1>\zeta]=\mathbb{E}_{r_1}[\mathcal{I}_1],\\&\mathbb{P}[\overline{\mathcal{A}}\cap\mathcal{B}]=(1-p_{\mathrm{to}})\left(1-\bar{p}_v^s\right),\mathbb{P}[\mathrm{SIR}_{\mathrm{sl}}^{k^*}>\zeta]=\mathbb{E}_{r_1}[\mathcal{I}_2],\\&\mathbb{P}[\overline{\mathcal{A}}\cap\overline{\mathcal{B}}]=(1-p_{\mathrm{to}})\,\bar{p}_v^s,\mathbb{P}[\mathrm{SIR}_{\mathrm{ml}}^{k^*}>\zeta]=\mathbb{E}_{r_1}[\mathcal{I}_3],\end{aligned} \tag{33}$$

where $\bar{p}_v^s=\int_0^\infty p_v^s(\eta)f_{\mathrm{SCIR}}(\eta)\,\mathrm{d}\eta$ is the average sensing error probability, and f_{SCIR} is the PDF of sensing SCIR in (21).

Proof. By averaging (28) over both r_1 and η, it follows that

$$\begin{aligned}p_{\mathrm{cov,C}}^{\mathrm{isac}}&=\int_0^\infty f_{r_1}(r_1)\int_0^\infty f_{\mathrm{SCIR}}(\eta)\,p_{\mathrm{cov,C}|r_1}^{\mathrm{isac}}(\zeta|\eta,r_1)\mathrm{d}\eta\mathrm{d}r_1\\&=p_{\mathrm{to}}\int_0^\infty f_{r_1}(r_1)\mathcal{I}_1\mathrm{d}r_1+(1-p_{\mathrm{to}})\left(1-\bar{p}_v^s(\eta)\right)\int_0^\infty f_{r_1}(r_1)\mathcal{I}_2\mathrm{d}r_1\\&+(1-p_{\mathrm{to}})\,\bar{p}_v^s(\eta)\int_0^\infty f_{r_1}(r_1)\mathcal{I}_3\mathrm{d}r_1.\end{aligned} \tag{34}$$

Comparing each term between (34) and (25), we can arrive at (33) and conclude the proof. □

We now characterize the asymptotic performance of the communication coverage probability in a special case.

Corollary 2. (SIR Coverage, Special Case) When $\alpha_L=\alpha_N=\alpha>2,\rho=n_B^2$, the asymptotic communication coverage probability is independent of λ_B and n_B

$$p_{\mathrm{cov,C}}^{\mathrm{isac},\infty}\to\left[1+\frac{2\pi}{\alpha}\csc\left(\frac{2\pi}{\alpha}\right)\zeta^{2/\alpha}-{}_2F_1\left(\frac{2}{\alpha},1;\frac{2}{\alpha}+1;-\frac{1}{\zeta}\right)\right]^{-1}, \tag{35}$$

where ${}_2F_1(\cdot,\cdot)$ is the Gauss hyper-geometric function.

Proof. First note that when $n_B\to\infty$, $p_{\mathrm{to}}=1-\exp(-n_B\sqrt{\lambda_B}v\tau_{\mathrm{RRC}}/\pi)\to1$. In such a case, there will be either no handover or beam assistance, and the MT always connects to the closest BS with sidelobe gain. Subsequently, only the first term in (34) exists. Rewrite (34) and (32)

$$p_{\mathrm{cov,C}}^{\mathrm{isac},\infty}\to\int_0^\infty U_{\mathrm{sl}}(\zeta,r_1^\alpha)f_{r_1}(r_1)\,\mathrm{d}r_1, \tag{36}$$

where

$$\begin{aligned}U_{\mathrm{sl}}(\zeta,r_1^\alpha)&=\exp\left[-2\pi\lambda_B\int_{r_1}^\infty\frac{w\zeta r_1^\alpha}{w^\alpha+\zeta r_1^\alpha}\mathrm{d}w\right]\\&\overset{(a)}{=}\frac{\zeta r_1^2}{\alpha}\left[\pi\csc\left(\frac{2\pi}{\alpha}\right)\zeta^{\frac{2}{\alpha}-1}-\frac{\alpha}{2\zeta}\,{}_2F_1\left(\frac{2}{\alpha},1;\frac{2}{\alpha}+1;-\frac{1}{\zeta}\right)\right],\end{aligned} \tag{37}$$

where (a) can be derived by letting $w=r_1s^{1/\alpha}$ and using (3.241) and (9.111) in [40]. Plugging this result into (36) gives the RHS of (35). □

Corollary 3. Under the same conditions as Corollary 2, there exists at least one $\tilde{n}_B<\infty$ such that $p_{\mathrm{cov,C}}^{\mathrm{isac}}(\zeta;\lambda_B,\lambda_O,\tilde{n}_B)>p_{\mathrm{cov,C}}^{\mathrm{isac},\infty}$, i.e., the optimal n_B is finite.

Proof. Consider the mainlobe communication coverage probability U_{ml} conditioning on r_1

$$\begin{aligned}U_{\mathrm{ml}}(\zeta,r_1^\alpha)&\approx\exp\left\{-2\pi\lambda_B\int_{r_1}^\infty\left[1-\frac{w^\alpha}{n_B(w^\alpha+\zeta r_1^\alpha)}-\frac{\rho w^\alpha}{\rho w^\alpha+\zeta r_1^\alpha}\right]w\mathrm{d}w\right\}\\&>\exp\left\{-2\pi\lambda_B\int_{r_1}^\infty\left[1-\frac{\rho w^\alpha}{\rho w^\alpha+\zeta r_1^\alpha}\right]w\mathrm{d}w\right\}\\&=\exp\left[-2\pi\lambda_B\int_{r_1}^\infty\frac{w\zeta r_1^\alpha}{\rho w^\alpha+\zeta r_1^\alpha}\mathrm{d}w\right]\overset{(b)}{>}U_{\mathrm{sl}}(\zeta,r_1^\alpha).\end{aligned} \tag{38}$$

Note that (b) comes simply from (37). When $n_B<\infty$, according to Lemma 1 and (29), we have $p_{\mathrm{to}}<1$ and $p_v^s<1$. This yields a positive contribution of U_{ml} to the total coverage probability (28). Since $U_{\mathrm{ml}}>U_{\mathrm{sl}}$, there always exists a $\tilde{n}_B<\infty$ satisfying that $p_{\mathrm{cov,C}}^{\mathrm{isac}}(\zeta;\lambda_B,\lambda_O,\tilde{n}_B)>p_{\mathrm{cov,C}}^{\mathrm{isac},\infty}$, which concludes the proof. □

Remark 4. Corollary 2 and 3 imply that, unlike sensing behavior, excessive beam numbers can be detrimental to communications. In fact, even if in the general case where $\alpha_N>\alpha_L\geq2$, the larger n_B or λ_B can increase the intensity of the beam switch and the probability of timeout, accordingly reducing the coverage. However, for a given ISAC network configuration specified by λ_B, λ_O, n_B, τ, and τ_{RRC}, the communication coverage probability ultimately depends only on the beam misalignment probability $\bar{p}_v^s$, which stems from sensing errors.

B. Optimal PRS Block Design

We now investigate the optimal PRS pilot pattern design that minimizes the error-induced beam misalignment probability p_v^s. Let the total pilot resource number of PRS be N_{re}, the time-to-frequency ratio be δ, so $T_{\mathrm{PRS}}=S_tN_{\mathrm{re}}^\delta T_{\mathrm{sym}},B_{\mathrm{PRS}}=S_fN_{\mathrm{re}}^{1-\delta}f_\Delta$. When the network parameters μ_g,μ_0,μ are given, the following minimum equivalence chain holds:

Lemma 3. (Minimization Equivalence Chain)

$$\min_{\delta,S_t,S_f}p_v^s(\eta)\overset{(a)}{\Longleftrightarrow}\min_{\delta,S_t,S_f}q(\sigma;\mu_g,\mu_0,\mu)\overset{(b)}{\Longleftrightarrow}\min_{\delta,S_t,S_f}\sigma^2.$$

Proof. Recall that $p_v^s(\eta)$ denotes the error-induced beam misalignment probability, and σ^2 denotes the sensing error variance. Since μ_g,μ_0,μ are given parameters in a specific setup, (a) holds naturally from (29). On the other hand, note that the integrating variable y in (27) satisfies $y-\mu\leq0$ in the range $[\mu_0,\mu]$, resulting in $\mathrm{erf}(\cdot)\leq0$. Hence, the monotonicity of q is kept the same as σ^2, which accounts for (b). □

Given the equivalence chain above, we derive the optimal pilot pattern in the following theorem.

Theorem 4. (Optimal Pilot Spacing and Allocation Ratio) The solution to the optimization problem

$$\min_{\delta,S_t,S_f}\left\{\sigma^2=\left(\frac{c\tau}{4\pi\eta f_c S_t T_{\rm sym} N_{\rm re}^{\delta}}\right)^2+2\left(\frac{\sin(\pi/n_B)c}{\eta S_f f_\Delta N_{\rm re}^{1-\delta}}\right)^2\right\},$$
$$\text{s.t. } \frac{c}{2f_c S_t T_{\rm sym}}\geq V_{\max}, \frac{c}{2f_\Delta S_f}\geq D_{\max}, 0<\delta<1, \tag{39}$$

is given by

$$S_t^*=\left\lfloor\frac{c}{2f_c T_{\rm sym} V_{\max}}\right\rfloor, S_f^*=\left\lfloor\frac{c}{2f_\Delta D_{\max}}\right\rfloor, \tag{40}$$

where $\lfloor\cdot\rfloor$ denotes the floor operator, and

$$\delta^*=\frac{1}{2}\left[\log_{N_{\rm re}}\left(\frac{\tau S_f^* f_\Delta}{4\sqrt{2}\pi\sin(\pi/n_B) f_c S_t^* T_{\rm sym}}\right)+1\right] \tag{41}$$

Proof. The expansion of σ^2 comes naturally from (13) and (30). First maximize the spacing values. Note that increasing the spacing S_t and S_f can yield a smaller fraction value, but, on the other hand, S_t and S_f are upper bounded by given constraints and must be integers, resulting in maximal integers they can achieve by (40). Subsequently, given the spacing values, the optimal value δ^* can be found using the property of an elementary inequality. □

Remark 5. (41) implies that the optimal time-frequency allocation ratio δ^* does not rely on the sensing SCIR η. Furthermore, since the center frequency f_c is very high in the mmWave and THz bands, the term $\log(\cdot)$ in (41) is negative. According to the property of the logarithm function, δ^* varies monotonically with $N_{\rm re}$. This suggests that systems with denser pilot configurations, i.e., larger $N_{\rm re}$, should prioritize time-domain resources, whereas sparse pilots benefit from frequency-domain allocation.

C. Beam Management Overhead and Effective ASE

1) Conventional Scheme: Beam management overhead quantifies the signaling resources consumed due to beam reselection and handover. The average beam reselection overhead of the conventional scheme is

$$T_{\rm overhead}^{\rm w/o}=\mu_b\cdot T_b+\mu_h\cdot T_h, \tag{42}$$

where μ_b is the beam reselection intensity, i.e., the number of beam reselections per unit time, T_b represents the overhead per beam reselection, $\mu_h=4v\sqrt{\lambda_B}/\pi$ is the time intensity of cell-level handovers, and T_h is the overhead per handover [41]. Considering the periodicity of the SSB τ, the observable frequency of beam selection is constrained by the periodic transmission of the SSBs. Therefore, the expression of μ_b is given by [4]

$$\mu_b=\left[\max\left(\tau,1/\mu_{t,b}\right)\right]^{-1}, \tag{43}$$

where $\mu_{t,b}=n_B\cdot v\sqrt{\lambda_B}/\pi$ is the geometry-based beam reselection intensity. Conventionally, a beam reselection takes one SSB period τ and one RRC processing delay $\tau_{\rm RRC}$, while a handover involves an extra random access channel (RACH) delay ($\tau_{\rm RACH}$ =20 ms). Hence, $T_b=\tau+\tau_{\rm RRC}$, and $T_h=T_b+\tau_{\rm RACH}$.

2) ISAC-enabled Scheme: Suppose the Extra SSB can be transmitted synchronously with the PRS block, the beam reselection overhead of the proposed ISAC scheme is[6]

$$T_{\rm overhead}^{\rm isac}=\underbrace{\mu_b^*\cdot T_b^*}_{\text{ISAC Beam Overhead}}+\underbrace{\mu_h^*\cdot T_h^*}_{\text{Extra HO Overhead}}+\mu_h\cdot T_h, \tag{44}$$

where $\mu_b^*=\left[\max\left(\tau_{\rm RRC},1/\mu_{t,b}\right)\right]^{-1}$, $T_b^*=T_{\rm PRS}+\tau_{\rm RRC}$, $\mu_h^*=\mu_h\bar{p}_{\rm HO}$, $T_h^*=T_b^*+\tau_{\rm RACH}$, and

$$\bar{p}_{\rm HO}=e^{-\mu v\tau_{\rm RRC}}\iint\limits_{0<r_1<r_2} p_N(r_1)\,p_L(r_2)\,f_{r_1,r_2}(r_1,r_2)\,{\rm d}r_1{\rm d}r_2$$

is the average handover probability.

Remark 6. (44) suggests the efficiency of ISAC in reducing overhead. For example, when $T_{\rm PRS}=5$ ms, $T_b^*=8$ ms, ISAC reduces more than 65% overhead compared to conventional $T_b=23$ ms. Although ISAC will introduce extra handovers and beam reselections, given that beam reselections occur far more frequently than handovers in multi-antenna systems, the ISAC-enabled beam management can significantly mitigate the overall overhead.

Finally, combining BS density, coverage probability, and overhead, the effective ASE is given as a comprehensive metric

$$\mathcal{R}_{\rm eff}(\lambda_B,\lambda_O,n_B)=\lambda_B(1-T_{\rm overhead})^+\mathcal{R}(\lambda_B,\lambda_O,n_B), \tag{45}$$

where

$$\mathcal{R}(\lambda_B,\lambda_O,n_B)=\frac{B_{\rm cb}}{\ln 2}\cdot\int_0^\infty p_{\rm cov,C}(\zeta;\lambda_B,\lambda_O,n_B)/(\zeta+1){\rm d}\zeta$$

is the ergodic Shannon rate [43] in bits per second (bps), $(x)^+=\max(x,0)$, $B_{\rm cb}$ denotes the carrier bandwidth, and $p_{\rm cov,C}$ is the communication coverage probability.

It should be noted that the derived ASE metric assumes the target BS has available resources to accommodate the handover or beam refinement requests. In a heavily loaded network, resource congestion at $\rm BS_2$ could lead to admission rejection. Consequently, the ASE values presented here serve as an upper bound on network capacity. However, in the dense deployment scenarios ($\lambda_B\geq 10^2/{\rm km}^2$) targeted by this work, the high degree of spatial reuse alleviates congestion probabilities. Furthermore, the relative ASE gain of the ISAC scheme is primarily driven by enhanced beam alignment probability and reduced physical layer overhead.

V. Numerical Results

To validate the theoretical analysis above, we consider the 5G-NR compliant RAN operating in a dense urban macro/pico cell scenario [4]. A summary of the model parameters for the mmWave and THz network deployments is shown in Table II.

A. Sensing Coverage Probability

We begin with the results of the sensing functionality, which has been analyzed in Theorem 1. Fig. 4 shows the sensing

[6]The uplink overhead associated with beam-reply and CSI feedback is typically conveyed over existing NR control channels and occupies only a small fraction of the resources used by downlink PRS/SSB patterns in dense deployments [42]. Such uplink signaling can be absorbed into the per-event overhead terms T_b^* and T_h^*. Since the proposed ISAC scheme reduces the number of beam reselections and handovers per UE, it also lowers the corresponding uplink beam-report overhead.

TABLE II: Network Parameter Settings

System Parameters	Scen. 1 (mmWave)	Scen. 2 (THz)
Center frequency (f_c) [4, 30]	30 GHz	100 GHz
Path loss exponent [30]	$\alpha_L = 2, \alpha_N = 3.3$	$\alpha_L = 2, \alpha_N = 4$
Default PRS duration (T_{PRS}) [22]	5 ms	1 ms
Default PRS bandwidth (B_{PRS}) [22]	240 MHz	
Carrier bandwidth (B_{cb}) [4]	400 MHz	
Symbol duration (T_{sym}) [44]	4.46 μs	
Subcarrier spacing frequency (f_Δ) [26]	240 kHz	
Node radius (r_O) [26]	1 m	
MT speed (v)	90 km/h	
SSB Periodicity (τ) [4]	20 ms	
RACH delay (τ_{RACH}) [4]	20 ms	
RRC delay (τ_{RRC}) [4]	3 ms	

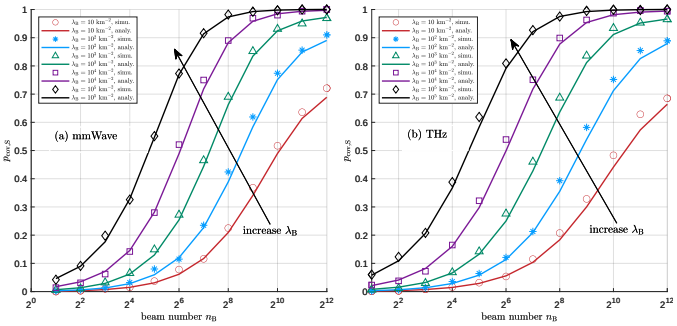

Fig. 4: Sensing SCIR coverage probability (η =0 dB).

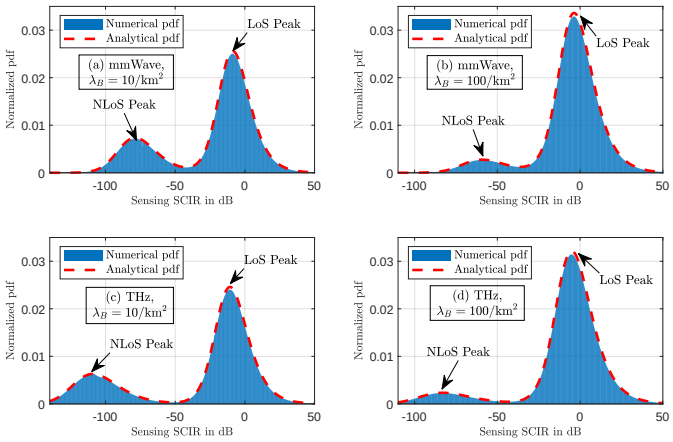

Fig. 5: Sensing SCIR PDFs with $n_B = 256$.

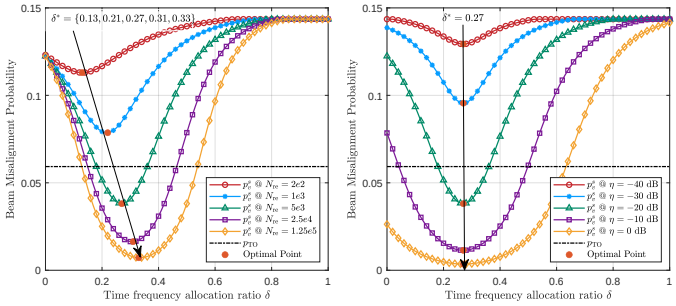

(a) mmWave, $\lambda_B = 10^2/\text{km}^2$, $D_{\max} = 150$ m, $v_{\max} = 120$ km/h.

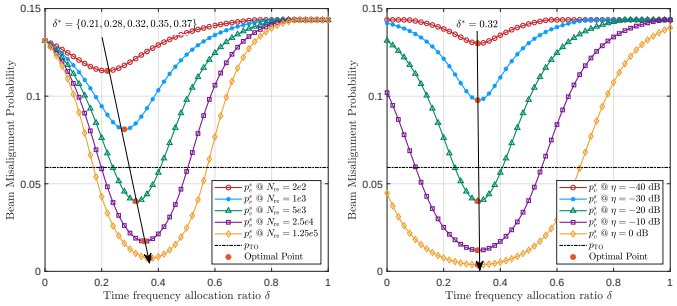

(b) THz, $\lambda_B = 10^3/\text{km}^2$, $D_{\max} = 200$ m, $v_{\max} = 100$ km/h.

Fig. 6: ISAC beam misalignment probability p_v^s with $n_B = 256$. Left: different resource element numbers; right: different sensing SCIRs.

SCIR coverage probability $p_{\text{cov,S}}$ as a function of the number of BS beams n_B for various BS densities λ_B and a fixed blockage density of $\lambda_O = 1000/\text{km}^2$ in the mmWave and THz regimes. It is evident that the analytical results by numerical integration closely align with the Monte Carlo simulation outcomes, validating the accuracy of the proposed analytical framework. We also observe that for every density, $p_{\text{cov,S}}$ increases monotonically with n_B, which is in agreement with our analysis in Remark 3. When $\lambda_B = 100/\text{km}^2$, increasing n_B from 128 to 1024 yields an approximate improvement of 0.2 in $p_{\text{cov,S}}$ for each doubling of n_B. Besides, increasing λ_B shifts the entire $p_{\text{cov,S}}$ versus n_B curve leftward and upward: For $n_B = 128$, when densifying BS from $\lambda_B = 10/\text{km}^2$ to $10^4/\text{km}^2$, $p_{\text{cov,S}}$ grows from around 0.2 to 0.75, corresponding to a doubling of $p_{\text{cov,S}}$ for every tenfold increase in λ_B. This is because the sensing signal undergoes a round-trip path loss, increasing λ_B confers more benefit than the interference it introduces, so the same coverage level can be reached with fewer beams.

In Fig. 5, we compare the simulated histograms of the sensing SCIR with the analytical PDFs obtained in (21) for a fixed beam number $n_B = 256$. The close alignment between the dashed red curves and the blue histograms in all four panels confirms the validity of the derived expressions. It can be seen from the results that each distribution is distinctly bimodal: the main peak at SCIR ≈ -5 dB represents LoS links, while the smaller peak near -90 dB is generated by NLoS paths. The increase in BS density from $\lambda_B = 10/\text{km}^2$ to $\lambda_B = 100/\text{km}^2$, i.e., from the subfigures (a) and (c) to (b) and (d), suppresses the peak of NLoS and sharpens the ridge of LoS, reflecting the shorter average distance of the link and the higher sensing quality in dense deployments. Comparing the mmWave and THz cases reveals slightly broader spectra and deeper NLoS dips in the THz band, capturing the harsher attenuation at higher carrier frequencies; nevertheless, the analytical PDF tracks the numerical result equally well in both bands and for both densities.

B. Communication Beam Misalignment and Coverage Probability

After analyzing the sensing performance, we proceed to investigate the communication component, with particular attention to beam misalignment and the resulting coverage performance. First, Fig. 6 shows the beam misalignment probability p_v^s as a function of the time–frequency allocation ratio $\delta \in (0, 1)$ for a fixed beam number $n_B = 256$, where the upper row corresponds to a mmWave cell density $\lambda_B = 10^2$ km^{-2} and the lower row to a THz density $\lambda_B = 10^3$ km^{-2} [27, 30]. The optimal δ^* derived in (41) is given in red-filled dots, and

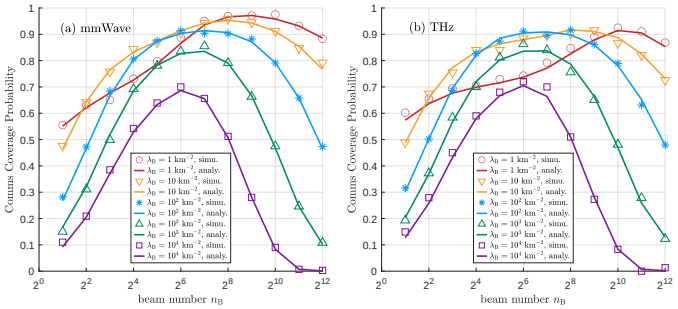

Fig. 7: Communication SIR coverage probability ($\eta = 0$ dB).

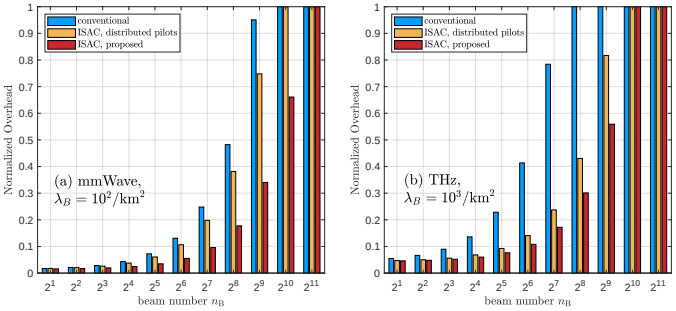

Fig. 8: The overheads comparison of different schemes.

the timeout probability p_{to} is also included as a benchmark. It is obvious that for each curve the dependence on δ is strictly convex, producing a single optimum $\delta^\star$, which matches well with analytical solutions. In addition, as given in Remark 5, when the number of PRS resource elements N_{re} increases (left panels), the optimal shifts from $\delta^\star \approx 0.13$ to 0.33 and the minimum value of p_v^s steadily decreases, which agrees with the analytical scaling derived in (41). In contrast, when the sensing SCIR η varies from -40 dB to 0 dB in fixed $N_{\text{re}} = 10^3$ (right panels), the curves move vertically, a higher η lowers the minimum probability of misalignment, but the optimum remains essentially constant around $\delta^\star \approx 0.27$ for mmWave and $\delta^\star \approx 0.32$ for THz, verifying that $\delta^\star$ is independent of η. When comparing the two frequency bands, the denser BS deployment in the THz bands yields a higher misalignment floor and a slightly larger optimal ratio because the narrower beams intensify beam-switching events. We can infer from this figure that while increasing the pilot resource number or sensing SCIR can indeed mitigate the beam misalignment probability, configuring the pilot properly makes sense as well.

Fig. 7 shows that the communication SIR coverage probability first increases and then decreases with the beam number n_B, demonstrating a bell-shaped curve for every λ_B in both scenarios. This can be explained as follows: When n_B is small, increasing n_B produces a higher beamforming gain, and this effect strengthens the desired signal faster than the interference, resulting in an increase in the coverage probability. However, as we illustrate in Remark 4, beyond an optimum value the trend reverses, as narrower beams shorten the beam switch distance d_b, increase the timeout probability p_{to}, and thus outweigh the beamforming benefit. It can also be seen that as λ_B increases from 1 to 100 km^{-2}, the optimal shifts to the left from roughly $n_B^* = 512$ to 128, and for the densest deployment $\lambda_B = 10^4\,\text{km}^{-2}$, the optimal n_B^* decreases to 64. Moreover, the THz curves attain slightly lower maxima than their mmWave counterparts for low-density BS deployments, reflecting stronger path loss at higher frequencies. We also observe that throughout the figure the analytical expressions computed as (34) lie nearly exactly on the Monte Carlo markers, which validates our analysis.

C. Beam Management Overhead and Effective ASE

Finally, and most importantly, we will compare and discuss the communication beam management overhead and the effective ASE under different schemes. Here, three schemes

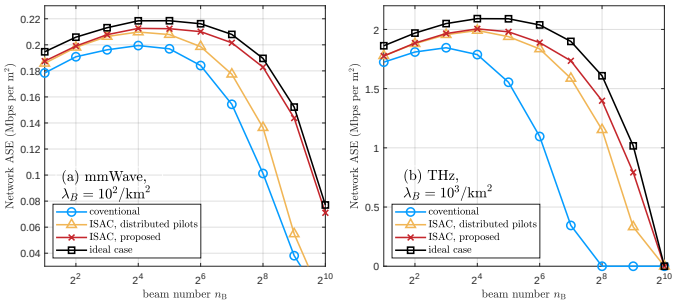

Fig. 9: The ASE comparison of different schemes.

are compared: conventional communication-only networks (labeled conventional), the ISAC scheme with distributed pilots [27] (labeled distributed pilots), and our proposed ISAC scheme. For a fair comparison, the resource element number is set to 5000, the pilot spacing value is set to 3, and other parameters remain the same as the previous settings. All three schemes are configured with the same total number of pilot resource elements and pilot energy. The distributed-pilot ISAC baseline [27] spreads these pilots uniformly over the entire frame, while the proposed scheme concentrates them into PRS blocks that are separated from data payloads. This configuration highlights the impact of pilot placement and beam-reselection dynamics, under a common pilot budget.

As shown in Fig. 8, the overheads of all three schemes grow exponentially with n_B due to the increasing frequency of beam switching and handover operations required by narrower beams. However, compared with conventional communication-only networks, ISAC shows its efficacy in mitigating the beam management overhead. When $n_B = 256$ in the mmWave scenario, the overhead of the conventional scheme is 0.48, and using the distributed pilot ISAC scheme [27] can reduce the overhead to 0.38, while our proposed ISAC scheme only consumes 0.17 overhead. The effect of the proposed scheme is more significant when it comes to the THz scenario, due to the higher BS density and more frequent beam-switch events. This is because the proposed scheme benefits from a shorter duration for sensing pilots given the total number of pilots, enabling more efficient beam assistance.

Fig. 9 shows the ASE curves for the aforementioned three schemes, while the ideal beamforming curve is introduced as a performance benchmark. Note that ASE also exhibits a bell-shaped dependence on n_B across all schemes, where performance first improves due to increased beamforming gain, but eventually declines as excessive overhead and beam misalignments accumulate. Apparently, the proposed ISAC

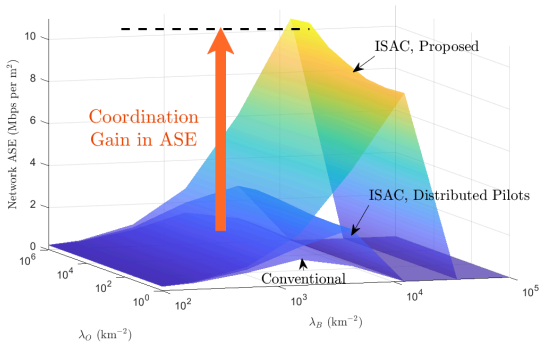

(a) mmWave, $n_B = 64$.

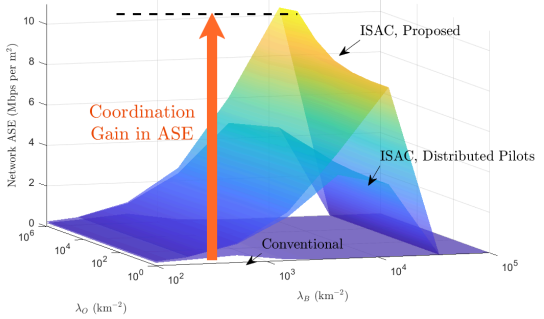

(b) THz, $n_B = 128$.

Fig. 10: The ASE comparison between conventional scheme and ISAC network under different BS and blockage densities.

consistently outperforms the conventional method, and the gain becomes more pronounced as n_B increases. For $n_B = 64$, ISAC shows a performance gain of 18.0% and 63.6% in two scenarios, respectively, which can support almost 4 times the number of beams compared to communication-only networks. Compared with the distributed pilot ISAC scheme [27], the proposed scheme has a gain from 16.7% to 28.5% when $n_B = 256$. This implies that although the proposed method sacrifices the duration of sensing (which leads to a loss in the velocity resolution), it shows an overall improvement in ASE due to the mitigated overhead.

Fig. 10 presents the network ASE performance as a 2-dimensional function of the base station density λ_B and the blocker density λ_O for the conventional and ISAC schemes under different configurations: the mmWave band with $n_B = 64$ and the THz band with $n_B = 128$. In both cases, the ASE shows a clear peak as λ_B varies, indicating the existence of an optimal deployment density that balances the desired signal power, interference, and blockage effects. In the conventional scheme, the maximum ASE reaches only 1.53 Mbps for mmWave and 0.48 Mbps for THz, and the ISAC scheme with distributed pilots [27] improves the ASE to 2.83 and 4.77 Mbps. In comparison, the proposed ISAC scheme significantly increases these maxima to 10.68 Mbps and 10.53 Mbps, respectively. This substantial improvement highlights the network-level coordination gain by using ISAC. Moreover, ISAC achieves its maximum ASE at a higher λ_B compared to the conventional scheme, reflecting its robustness against increased interference due to better beam alignment, blockage awareness, and overhead reduction. Another interesting yet counterintuitive finding is that an increase in blockage density λ_O can sometimes be beneficial (although this effect is subtle compared to the change in λ_B), as has also been reported in [29]. This can be explained by two reasons: (1) the blockage can avoid interference from adjacent cells; (2) given high BS density, the desired link suffers less blockage effect than interference links because of the proactive handover in the proposed ISAC scheme.

In summary, we have validated that the proposed ISAC scheme can significantly reduce beam management overheads and enhance the network spectral efficiency, especially in the presence of large antenna numbers and/or high BS densities. These findings not only verify the analytical framework, but also give practical insight for network deployments.

While this work focuses on a single-user downlink scenario to facilitate tractable analysis, the proposed framework can be extended to multi-user or uplink scenarios. In a multi-user system, the BS allocates time-frequency resources to multiple MTs. Although this introduces scheduling constraints and varying interference patterns, the fundamental trade-off between beamwidth and alignment probability for each link remains governed by the mobility dynamics analyzed here. As a result, the optimal pilot design strategy would likely involve a joint optimization of resource blocks across users. For uplink transmission, time division duplex (TDD) systems can also exploit channel reciprocity, allowing the MT to utilize the beam direction estimated by the BS's downlink sensing, potentially reducing the uplink pilot overhead. Future work will formally model these multi-user scheduling and uplink reciprocity effects.

VI. Conclusion

This paper develops a comprehensive ISAC-enabled framework to enhance the coverage performance of the mmWave/THz communication network. We first proposed a 5G-NR-based ISAC beam management architecture with dedicated sensing signals. Using SG, the proposed model effectively captures key system dynamics, including beam misalignment, blockage effects, and handover overheads. Tractable expressions are derived for the ISAC-enabled coverage probability and the effective ASE of the network. Furthermore, we have given the closed-form solutions to the optimal pilot pattern design. Our findings reveal the fundamental tradeoff between beamforming gain and mobility-induced misalignment, identifying an optimal beam number that maximizes spectral efficiency. On the one hand, the proposed ISAC beam management scheme can be applied in the design of next-generation wireless networks, especially in scenarios requiring ultra-dense base station deployment, high-frequency operation, or environments with severe blockage. On the other hand, the analytical framework provides a guide for configuring beam management parameters and resource allocation in practical ISAC systems. Future work may extend this framework to multi-user and multi-cell coordination, integrate more realistic sensing models, and explore adaptive beam management strategies under dynamic network conditions.

APPENDIX A
PROOF OF THEOREM 1

From (16) and SCIR formulation (7), it follows that

$$\begin{aligned}
&p_{\mathrm{cov,s}}\left(\eta|r_1\right)=\mathbb{P}\left(\mathrm{SCIR_S}>\eta|r_1\right)\\
&=\mathbb{P}\Big(\frac{P_{\mathrm{S}}G_{\mathrm{ml}}\sigma_{\mathrm{M}}\mathcal{L}_{\mathrm{rt}}\left(r_1\right)}{\sum_i P_{\mathrm{S}}h_iL\left(\ell_i\right)G_{\mathrm{S}}^{\mathrm{I}}(\phi_i)+\sum_{ct\in R_{\mathrm{M}}}P_{\mathrm{S}}G_{\mathrm{ml}}\sigma_{\mathrm{CT}}\mathcal{L}_{\mathrm{rt}}(r_1)}>\eta|r_1\Big)\\
&\overset{(a)}{=}\mathbb{E}\Big[\exp\Big(-\eta\frac{\sum_i h_iL(\ell_i)G_{\mathrm{S}}^{\mathrm{I}}(\phi_i)+N_{\mathrm{CT}}G_{\mathrm{ml}}\sigma_{\mathrm{CT}}\mathcal{L}_{\mathrm{rt}}(r_1)}{G_{\mathrm{ml}}\,\mathcal{L}_{\mathrm{rt}}(r_1)}\Big)\Big]\\
&=\underbrace{\mathbb{E}\Big[\exp\Big(-\eta\sum_{ct=1}^{N_{\mathrm{CT}}}\sigma_{\mathrm{CT}}\Big)\Big]}_{\text{A. Clutter Factor}}\underbrace{\mathbb{E}\Big[\exp\Big(-\eta\frac{\sum_i h_iL(\ell_i)G_{\mathrm{S}}^{\mathrm{I}}(\phi_i)}{G_{\mathrm{ml}}\,\mathcal{L}_{\mathrm{rt}}(r_1)}\Big)\Big]}_{\text{B. Sensing SIR Coverage}},
\end{aligned}\tag{46}$$

where (a) is because $\sigma_{\mathrm{M}}\sim\exp(1)$, and N_{CT} denotes the number of clutter in the resolution cell. For clutter term A, since $\sigma_{\mathrm{CT}}\sim\exp(1)$, we have

$$F_{ct}\triangleq \mathrm{A}=\mathbb{E}\left[\sum_{ct=1}^{N_{CT}}\frac{1}{1+\eta}\right]\overset{(b)}{=}\exp\left(-\frac{2\pi\eta\lambda_{\mathrm{O}}r_1\Delta r}{n_{\mathrm{B}}(1+\eta)}\right),\tag{47}$$

where (b) is derived using the probability-generating functional (PGFL) of PPP and $A(R_{\mathrm{M}})\approx 2\pi\Delta r\cdot r_1/n_B$, and

$$\begin{aligned}
\mathrm{B}&\overset{(c)}{=}\mathbb{E}_{L,\mathcal{L}_{\mathrm{rt}}}\left\{\prod_i\left[1+\frac{\eta L\left(\ell_i\right)G_{\mathrm{S}}^{\mathrm{I}}\left(\phi_i\right)}{G_{\mathrm{ml}}\mathcal{L}_{\mathrm{rt}}\left(r_1\right)}\right]^{-1}\right\}\\
&\overset{(d)}{=}p_L\left(r_1\right)F_{S,L}(\eta|r_1)+p_N\left(r_1\right)F_{S,N}(\eta|r_1),
\end{aligned}\tag{48}$$

where (c) is by averaging over all fading interfering paths h_i. (d) uses the path loss probability mass function (PMF) of the desired link with distance r_1, and interferes with the link with distance ℓ_i. Conditioning on the LoS desired link, we can use the PMF of $G_{\mathrm{S}}^{\mathrm{I}}(\cdot)$ to compute

$$\begin{aligned}
&F_{S,L}(\eta\mid r_1)\\
&\triangleq\prod_i\Bigg\{p_L(\ell_i)\left[\frac{1/n_B^2}{1+4\pi\eta\ell_i^{-\alpha_L}r_1^{2\alpha_L}}+\frac{1-1/n_B^2}{1+\left(4\pi\eta\ell_i^{-\alpha_L}r_1^{2\alpha_L}\right)/\rho}\right]\\
&+p_N(\ell_i)\left[\frac{1/n_B^2}{1+4\pi\eta\ell_i^{-\alpha_N}r_1^{2\alpha_L}}+\frac{1-1/n_B^2}{1+\left(4\pi\,\eta\,\ell_i^{-\alpha_N}\,r_1^{2\alpha_L}\right)/\rho}\right]\Bigg\}.\\
&\overset{(e)}{=}\exp\left[-2\lambda_B\pi\int_0^{\infty}w\left(1-Q\left(w,r_1^{2\alpha_L}\right)\right)\mathrm{d}w\right],
\end{aligned}\tag{49}$$

where (e) uses the PGFL of PPP again, and the function $Q(\cdot,\cdot)$ follows the form in the brace by replacing the variable ℓ_i with w. Similarly, $F_{S,N}$ can be derived.

APPENDIX B
PROOF OF THEOREM 2

We first derive the sensing error-induced beam misalignment probability p_v^s conditioning on no timeout. By definition, this happens when $d_b<v\tau$ while estimate value $\hat{d}_b>\hat{v}\tau$. Formally, we write:

$$\begin{aligned}
&\mathbb{P}\left[d_b<v\tau,\hat{d}_b>\hat{v}\tau\ |d_b>v\tau_{\mathrm{RRC}}\right]\\
&=\mathbb{P}\left[\left(v+\epsilon_v\right)\tau-\epsilon_d<d_b<v\tau\ |d_b>v\tau_{\mathrm{RRC}}\right]\\
&=\mathbb{P}\left[\max\left(X,\mu_0\right)<Y<\mu\ \right]/\mathbb{P}\left(Y>\mu_0\right)\\
&\overset{(a)}{=}q(\sigma(\eta);\mu_g,\mu_0,\mu)e^{\mu_g\mu_0},
\end{aligned}\tag{50}$$

where the variables are simplified according to (30), and step (a) follows from Lemma 2. Comparing this probability with the conventional beam misalignment probability leads to (29)[7].

Next, we provide a proof sketch of (31) and (32). Let $U_\Omega(\zeta,r_k^\alpha),\Omega\in\{\mathrm{ml},\mathrm{sl}\}$ denote the coverage probability, and $r_k,k\in\{1,2\}$ denote the distance between BS_k and MT. First, in case of timeout event $\mathcal{A}$, the MT can only connect to BS_1 with sidelobe gain, corresponding to $\mathcal{I}_1$ in (31).

Second, if no timeout occurs, the ISAC-enabled handover scheme allows the MT to compare the link qualities of the two closest BSs and select the better link. Note that proactive handover is triggered only when link 1 experiences an NLoS condition and link 2 is in LoS; otherwise, the MT always connects to link 2. Conditioning on r_1, we can accordingly write the coverage probability $W_\Omega(r_2;r_1)$ in a three-fold form by considering all the possibilities of link state, which is given by (32a). The expressions in (32c) and (32d) follow by similar derivations as in Appendix A, which are omitted here. Moreover, $\mathcal{I}_2$ corresponds to the coverage of the mainlobe with correct beam assistance averaging over r_2, while $\mathcal{I}_3$ corresponds to the coverage of the sidelobe as the sensing error affects the assistance decision. Thus, the proof can be concluded by combining the above results.

REFERENCES

[1] W. Saad, M. Bennis, and M. Chen, "A Vision of 6G Wireless Systems: Applications, Trends, Technologies, and Open Research Problems," *IEEE Network*, vol. 34, no. 3, pp. 134–142, 2020.

[2] T. S. Rappaport, S. Sun, R. Mayzus, H. Zhao, Y. Azar, K. Wang, G. N. Wong, J. K. Schulz, M. Samimi, and F. Gutierrez, "Millimeter Wave Mobile Communications for 5G Cellular: It Will Work!" *IEEE Access*, vol. 1, pp. 335–349, 2013.

[3] S. Rangan, T. S. Rappaport, and E. Erkip, "Millimeter-Wave Cellular Wireless Networks: Potentials and Challenges," *Proceedings of the IEEE*, vol. 102, no. 3, pp. 366–385, 2014.

[4] S. S. Kalamkar, F. Baccelli, F. M. Abinader, A. S. M. Fani, and L. G. U. Garcia, "Beam Management in 5G: A Stochastic Geometry Analysis," *IEEE Transactions on Wireless Communications*, vol. 21, no. 4, pp. 2275–2290, 2022.

[5] F. Liu, Y. Cui, C. Masouros, J. Xu, T. X. Han, Y. C. Eldar, and S. Buzzi, "Integrated Sensing and Communications: Toward Dual-Functional Wireless Networks for 6G and Beyond," *IEEE Journal on Selected Areas in Communications*, vol. 40, no. 6, pp. 1728–1767, 2022.

[6] D. K. Pin Tan, J. He, Y. Li, A. Bayesteh, Y. Chen, P. Zhu, and W. Tong, "Integrated Sensing and Communication in 6G: Motivations, Use Cases, Requirements, Challenges and Future Directions," in *2021 1st IEEE International Online Symposium on Joint Communications & Sensing (JC&S)*, 2021, pp. 1–6.

[7]This can be implemented by an error-aware scheme: if the sensing SCIR falls below a predefined threshold, the system deactivates beam assistance.

[7] J. A. Zhang, F. Liu, C. Masouros, R. W. Heath, Z. Feng, L. Zheng, and A. Petropulu, "An Overview of Signal Processing Techniques for Joint Communication and Radar Sensing," *IEEE Journal of Selected Topics in Signal Processing*, vol. 15, no. 6, pp. 1295–1315, 2021.

[8] W. Yuan, F. Liu, C. Masouros, J. Yuan, D. W. K. Ng, and N. González-Prelcic, "Bayesian Predictive Beamforming for Vehicular Networks: A Low-Overhead Joint Radar-Communication Approach," *IEEE Transactions on Wireless Communications*, vol. 20, no. 3, pp. 1442–1456, 2021.

[9] C. Liu, W. Yuan, S. Li, X. Liu, H. Li, D. W. K. Ng, and Y. Li, "Learning-Based Predictive Beamforming for Integrated Sensing and Communication in Vehicular Networks," *IEEE Journal on Selected Areas in Communications*, vol. 40, no. 8, pp. 2317–2334, 2022.

[10] Y. Li, F. Liu, Z. Du, W. Yuan, and C. Masouros, "ISAC-Enabled V2I Networks Based on 5G NR: How Much Can The Overhead Be Reduced?" in *2023 IEEE International Conference on Communications Workshops (ICC Workshops)*. IEEE, 2023, pp. 691–696.

[11] U. Demirhan and A. Alkhateeb, "Integrated Sensing and Communication for 6G: Ten Key Machine Learning Roles," *IEEE Communications Magazine*, vol. 61, no. 5, pp. 113–119, 2023.

[12] A. Liu, M. Li, M. Kobayashi, and G. Caire, "Fundamental Limits for ISAC: Information and Communication Theoretic Perspective," in *Integrated Sensing and Communications*. Springer, 2023, pp. 23–52.

[13] Y. Xiong, F. Liu, Y. Cui, W. Yuan, T. X. Han, and G. Caire, "On The Fundamental Tradeoff of Integrated Sensing and Communications under Gaussian Channels," *IEEE Transactions on Information Theory*, vol. 69, no. 9, pp. 5723–5751, 2023.

[14] Z. Du, F. Liu, Y. Xiong, T. X. Han, Y. C. Eldar, and S. Jin, "Reshaping The ISAC Tradeoff under OFDM Signaling: A Probabilistic Constellation Shaping Approach," *IEEE Transactions on Signal Processing*, 2024.

[15] M. Ahmadipour and M. Wigger, "An Information-Theoretic Approach to Collaborative Integrated Sensing and Communication for Two-Transmitter Systems," *IEEE Journal on Selected Areas in Information Theory*, vol. 4, pp. 112–127, 2023.

[16] N. R. Olson, J. G. Andrews, and R. W. Heath, "Coverage and Rate of Joint Communication and Parameter Estimation in Wireless Networks," *IEEE Transactions on Information Theory*, vol. 70, no. 1, pp. 206–243, 2023.

[17] J. Xu, M. A. Kishk, J. P. Coon, and M.-S. Alouini, "Performance Analysis and Optimal Resource Allocation for Large Scale Joint Sensing and Communication," *IEEE Transactions on Wireless Communications*, vol. 23, no. 10, pp. 14 350–14 364, 2024.

[18] X. Gan, C. Huang, Z. Yang, X. Chen, J. He, Z. Zhang, C. Yuen, Y. Liang Guan, and M. Debbah, "Coverage and Rate Analysis for Integrated Sensing and Communication Networks," *IEEE Journal on Selected Areas in Communications*, vol. 42, no. 9, pp. 2213–2227, 2024.

[19] Y. Nabil, H. ElSawy, S. Al-Dharrab, H. Mostafa, and H. Attia, "Beamwidth Design Tradeoffs in Radar-Aided Millimeter-Wave Cellular Networks: A Stochastic Geometry Approach," *IEEE Access*, 2024.

[20] K. Meng, C. Masouros, G. Chen, and F. Liu, "Network-Level Integrated Sensing and Communication: Interference Management and BS Coordination Using Stochastic Geometry," *IEEE Transactions on Wireless Communications*, 2024.

[21] Z. Wei, H. Qu, Y. Wang, X. Yuan, H. Wu, Y. Du, K. Han, N. Zhang, and Z. Feng, "Integrated Sensing and Communication Signals Toward 5G-A and 6G: A Survey," *IEEE Internet of Things Journal*, vol. 10, no. 13, pp. 11 068–11 092, 2023.

[22] Z. Wei, Y. Wang, L. Ma, S. Yang, Z. Feng, C. Pan, Q. Zhang, Y. Wang, H. Wu, and P. Zhang, "5G PRS-Based Sensing: A Sensing Reference Signal Approach for Joint Sensing and Communication System," *IEEE Transactions on Vehicular Technology*, vol. 72, no. 3, pp. 3250–3263, 2023.

[23] Z. Zhang, H. Ren, C. Pan, S. Hong, D. Wang, J. Wang, and X. You, "Target Localization in Cooperative ISAC Systems: A Scheme Based on 5G NR OFDM Signals," *IEEE Transactions on Communications*, 2024.

[24] K. Patel and R. W. Heath, "Harnessing Multimodal Sensing for Multi-User Beamforming in Mmwave Systems," *IEEE Transactions on Wireless Communications*, vol. 23, no. 12, pp. 18 725–18 739, 2024.

[25] X. Qian, X. Hu, C. Liu, M. Peng, and C. Zhong, "Sensing-Based Beamforming Design for Joint Performance Enhancement of RIS-Aided ISAC Systems," *IEEE Transactions on Communications*, vol. 71, no. 11, pp. 6529–6545, 2023.

[26] W. Chen, L. Li, Z. Chen, T. Quek, and S. Li, "Enhancing THz/Mmwave Network Beam Alignment with Integrated Sensing and Communication," *IEEE Communications Letters*, vol. 26, no. 7, pp. 1698–1702, 2022.

[27] W. Chen, L. Li, Z. Chen, Y. Liu, B. Ning, and T. Q. S. Quek, "ISAC-Enabled Beam Alignment for Terahertz Networks: Scheme Design and Coverage Analysis," *IEEE Transactions on Vehicular Technology*, vol. 73, no. 12, pp. 19 019–19 033, 2024.

[28] S. Zuyev, "Strong Markov Property of Poisson Processes and Slivnyak Formula," *Case studies in spatial point process modeling*, pp. 77–84, 2006.

[29] T. Bai, R. Vaze, and R. W. Heath, "Analysis of Blockage Effects on Urban Cellular Networks," *IEEE Transactions on Wireless Communications*, vol. 13, no. 9, pp. 5070–5083, 2014.

[30] D. Moltchanov, E. Sopin, V. Begishev, A. Samuylov, Y. Koucheryavy, and K. Samouylov, "A Tutorial on Mathematical Modeling of 5G/6G Millimeter Wave and Terahertz Cellular Systems," *IEEE Communications Surveys & Tutorials*, vol. 24, no. 2, pp. 1072–1116, 2022.

[31] Z. Sun, S. Yan, N. Jiang, J. Zhou, and M. Peng, "Performance Analysis of Integrated Sensing and Communication Networks with Blockage Effects," *IEEE Transactions on Vehicular Technology*, vol. 73, no. 11, pp. 16 876–16 891, 2024.

[32] E. Björnson, J. Hoydis, M. Kountouris, and M. Debbah, "Massive MIMO Systems With Non-Ideal Hardware: Energy Efficiency, Estimation, and Capacity Limits," *IEEE Transactions on Information Theory*, vol. 60, no. 11, pp. 7112–7139, 2014.

[33] "3GPP TR 38.855: Study on NR Positioning Support," 3GPP, Tech. Rep. TR 38.855 V16.0.0, 2019, release 16. [Online]. Available: https://atisorg.s3.amazonaws.com/archive/3gpp-documents/Rel16/ATIS.3GPP.38.855.V1600.pdf

[34] Ericsson, "RRC UE Processing Time for Standalone NR to Reach ITU Target," 3GPP TSG-RAN WG2 Meeting 101, R2-1805446, 2018. [Online]. Available: https://www.3gpp.org/ftp/tsg_ran/WG2_RL2/TSGR2_101bis/Docs/R2-1805446.zip

[35] S. S. Ram, G. Singh, and G. Ghatak, "Optimization of Radar Parameters for Maximum Detection Probability under Generalized Discrete Clutter Conditions Using Stochastic Geometry," *IEEE Open Journal of Signal Processing*, vol. 2, pp. 571–585, 2021.

[36] M. A. Richards, J. Scheer, W. A. Holm, and W. L. Melvin, *Principles of Modern Radar*. SciTech Publishing Inc., 2010.

[37] D. Barton, "Radar System Analysis and Modeling," *IEEE Aerospace and Electronic Systems Magazine*, vol. 20, no. 4, pp. 23–25, 2005.

[38] K. M. Braun, "OFDM Radar Algorithms in Mobile Communication Networks," Ph.D. Dissertation, Karlsruhe Institute of Technology (KIT), Karlsruhe, Germany, 2014.

[39] H. You, Z. Hongwei, and T. Xiaoming, "Joint Systematic Error Estimation Algorithm for Radar and Automatic Dependent Surveillance Broadcasting," *IET Radar, Sonar & Navigation*, vol. 7, no. 4, pp. 361–370, 2013.

[40] I. S. Gradshteyn and I. M. Ryzhik, *Table of Integrals, Series, and Products*. Academic Press, 2014.

[41] F. Baccelli and S. Zuyev, "Stochastic Geometry Models of Mobile Communication Networks," in *Frontiers in Queueing*, J. D. Little, Ed. Boca Raton, FL, USA: CRC Press, 1997, pp. 227–243.

[42] "3GPP TR 38.824: Study on Physical Layer Enhancements for NR Ultra-Reliable and Low Latency Case (URLLC)," 3GPP, Tech. Rep. TR 38.824 V16.0.0, 2020, release 16. [Online]. Available: https://www.tech-invite.com/3m38/tinv-3gpp-38-824.html

[43] J. G. Andrews, F. Baccelli, and R. K. Ganti, "A Tractable Approach to Coverage and Rate in Cellular Networks," *IEEE Transactions on Communications*, vol. 59, no. 11, pp. 3122–3134, 2011.

[44] M. H. C. Garcia, A. Molina-Galan, M. Boban, J. Gozalvez, B. Coll-Perales, T. Şahin, and A. Kousaridas, "A Tutorial on 5G NR V2X Communications," *IEEE Communications Surveys & Tutorials*, vol. 23, no. 3, pp. 1972–2026, 2021.